Computational modeling of biological molecule separation in nanofluidic devices

by

Ghassan N. Fayad

B.S., Mechanical Engineering, University of Balamand, Lebanon (2003)
M.S., Civil and Structural Engineering, University of Maine (2005)
M.S., Mechanical Engineering, University of Maine (2005)

Submitted to the Department of Mechanical Engineering
in partial fulfillment of the requirements for the degree of

Doctor of Philosophy in Mechanical Engineering

at the

MASSACHUSETTS INSTITUTE OF TECHNOLOGY

June 2010

Author ....
Department of Mechanical Engineering
May 21, 2010

Certified by ....
Nicolas G. Hadjiconstantinou
Associate Professor, Mechanical Engineering
Thesis Supervisor

Accepted by ....
David E. Hardt
Chairman, Department Committee on Graduate Students

Computational modeling of biological molecule separation in nanofluidic devices

by

Ghassan N. Fayad

Submitted to the Department of Mechanical Engineering
on May 21, 2010, in partial fulfillment of the
requirements for the degree of
Doctor of Philosophy in Mechanical Engineering

Abstract

Separation of biological molecules such as DNA and protein is of great importance for the chemical and pharmaceutical industries. In recent years, several researchers focused on fabricating patterned regular sieving nanostructures instead of using porous gel media to separate various types of biological molecules. Theoretical modeling of the separation process is very desirable for gaining fundamental understanding, device optimization and parameter exploration.

Despite their small sizes, these devices contain a very large number of solvent molecules making ab-initio molecular modeling intractable. In other words, for an efficient model, some degree of coarse-graining is required. In this Thesis, we focus on the development of Brownian Dynamics (BD) simulation tools for modeling the performance of nanofluidic devices for the separation of short, Ogston-regime, dsDNA molecules.

The first part of this Thesis focuses on the development of Brownian Dynamics models to predict the electrophoretic velocity of dsDNA molecules in nanoscale separation devices. The most general model developed here is based on the *Worm-Like-Chain* (WLC) model which includes the effects of bending and stretching stiffness and provides the most accurate mechanical description of the DNA molecule. The resulting Brownian Dynamics formulation includes hydrodynamic interactions within the molecule, and closely models the experimental set up of Fu et al. whose data are used for validation. For molecules that are sufficiently short (length on the order of, or smaller than, the persistence length), we developed a BD model which treats DNA molecules as rigid rods; this results in significantly reduced computational requirements. Finally, we present a further simplified BD model which treats the DNA molecules as point particles while accounting for their orientational degrees of freedom through an entropic energy barrier. This model is the most efficient and simplest to implement, but also is limited to short, essentially rigid molecules. Both the rigid-rod and the point particle model agree well with the experimental data of Fu et al. for appropriately short molecules.

In the second part of this Thesis we present a variance reduction methodology for reducing the statistical uncertainty of Brownian Dynamics simulations. Our formulation is based on the recent method of Al-Mohssen and Hadjiconstantinou which uses importance weights within a control variate formulation. Variance reduction is achieved by subtracting the results of an equilibrium simulation using the same random numbers from the non-equilibrium results. Significant variance reduction is achieved for small electric fields, while very little additional computational cost is incurred.

Thesis Supervisor: Nicolas G. Hadjiconstantinou
Title: Associate Professor, Mechanical Engineering

Biography

Ghassan Fayad was born in 1982 in Kafaraakka – Koura, Lebanon. He has had a passion for mathematics and a deep fascination with science and its applications since his childhood. He graduated with high distinction from Saint Thérèse High School, Amioun – Koura, Lebanon in 2000 with an emphasis in mathematics. He received a Bachelor of Science in Mechanical Engineering with high distinction from the University of Balamand, Lebanon in 2003. There he was recognized as the top graduate in the college of engineering in 2003. He came to Maine, USA on August 25, 2003 to receive a dual degree, Master of Science in Civil and Structural Engineering and Master of Science in Mechanical Engineering in May, 2005. Later, in August 2005, he entered the Ph.D. program in the Mechanical Engineering department at the Massachusetts Institute of Technology (MIT). Ghassan is passionate about teaching, and has facilitated student learning in physics, math, and engineering at University of Balamand, University of Maine and MIT. His honors include first place at MIT 50K Arab Business Plan Competition in 2009; American Lebanese Engineering Society, Charles Zraket Scholarship Award in 2006; University of Balamand Founder's Award in 2003; and University of Balamand, Professors of the Faculty of Engineering Student Excellence Award in 2003. Ghassan currently lives in Cambridge, MA. After, finishing his graduate studies at MIT, Ghassan will be pursuing his passion for research and science by joining the Applied Computer Science and Mathematics Department (ACSM) at Merck & Co. as a research associate.

Acknowledgments

My time spent in Cambridge, Massachusetts was only improved by the people I worked with and got to know while I was here. A significant portion of my enjoyment comes from the hard work and dedication of my Thesis supervisor, Professor Nicolas G. Hadjiconstantinou. I would like to thank Professor Hadjiconstantinou for his advice, patience, professional guidance, technical expertise, creative ideas, flexibility, promptness and generosity in allowing me to pursue my own ideas and research directions while keeping me on track. I will forever be grateful to him for giving me increasing levels of responsibility as my graduate experience progressed. I very much enjoyed working under his supervision and assisting him in teaching two classes. I learned a lot from him throughout these five years.

I would like to thank my committee member Professor Gareth H. McKinley for his enthusiasm, constant support, professional advice and allowing me to attend his summer research group readings that helped me broaden my horizons. I would like to thank Professor Jongyoon Professor for serving on my thesis committee and his research group (Dr. Jianping Fu in particular), for making their experimental data available and for useful discussions. Thank you to Dr. Zi Rui Li for his professional advice and fruitful research discussions. This work was supported by the Singapore-MIT alliance (SMA-II, CE program).

Professor Rohan Abeyaratne, thank you for your calming advice and support whenever I needed it. I very much enjoyed the "Coffee Hour with Rohan" and occasionally meeting with you for general advice.

Professor Anthony Patera, I very much enjoyed working for you as a teaching assistant for two semesters, I learned a lot from your teaching expertise and very much enjoyed running the lab and teaching young minds science, engineering and numerical methods.

Professor Henrik Schmidt, I really enjoyed working for you as a teaching assistant for one semester, and enjoyed learning about acoustic rays.

Justin Kao, it was a pleasure working with you teaching undergraduate students and learning cool Linux tricks.

Thank you to Professor Patrick Doyle and Dr. Patrick Underhill for their advice about Brownian Dynamics simulation.

Professor Borivoje (Bora) Mikic, thank you for your general advice and support.

My education at MIT was enriched by interaction with fellow students and friends. I am especially grateful to my office mates (Husain Al-Mohssen, Lowell Baker, Thomas Homolle, Saeed Bagheri, Gregg Radtke, Colin Landon, Jean-Philippe Peraud, Ho-Man Lui and Lian Zhengyi) for their support and assistance.

Many thanks to my wonderful roommates: Guo Qiang, Costas Pelekanakis and Sherif Kassatly.

Maria de Soria-Santacruz Pich (MdS), you spent hours working next to me in the library while writing this Thesis. Thank you for your support.

I would like to also thank my friends that I met throughout my stay at MIT, namely: Fabio Fachin, Ghassan Moussa, Sherif Kassatly, Randy Ewoldt, Alex Al-Massih, Rami El-Hayek, Joseph Halabi, Anwar Ghosh, Francesco Mazzini, Henri Badaro, Georges Aoude, John Boghossian, Mirna Slim, Alice Nawfal, Carine Abi Akar, Zeina Saab, Nader Shaar, Hussam Zebian, Daniel Massimini, Ghinwa Choueiter, Samir Mikati, Bahjat Dagher, Said Francis, Fadi Kanaan, Zahi Karam, Joe Khoury, Rami Rahal, Cyril Koniski, Loai Naamani, Mesrob Ohannessian, Loai Naamani, Dana Najjar, Daniele Diab, Danielle Issa, Dimitrios Tzeranis, Stephanie Gil, Carolina Moraes, François Le Floch, Reza Alam, Carolina Moraes, Luciana Pereira, Maria-Eirini Alexandraki, Stavros Valavanis, Ioannis Bertsatos, and many others for creating a joyful and unforgettable five years in Cambridge/Boston for me.

Thank you to my qualifying exam study group members: Siddarth Kumar, Mayank Kumar, Feras Eid and Gregg Radtke.

Thank you to the Syphir team (Husain A. Al-Mohssen, Courtland Allen, Abdulrahman Tarbzouni and Faisal Alibrahim) for winning the first place at MIT 50K Arab Business Plan Competition. It was a wonderful challenging and learning experience.

I am also grateful to the staff of Mechanical Engineering Department, especially Leslie Regan, Joan Kravit, Deborah Alibrandi and Debra Blanchard for providing a

nice relaxing academic environment. Their support and efforts are greatly appreciated.

I would like to use this opportunity to thank my undergraduate advisors, Professor Elie Honein and Professor Habib Rai for shaping my career path and constantly supporting me and encouraging me. Also I am grateful to Professor Michel Najjar and Professor Elie Salem for many helpful discussions. Also, many thanks to my master advisors at the University of Maine Professor Habib Dagher and Professor Roberto Lopez-Anido for their support and encouragement to join MIT for my doctoral degree.

I am ultimately indebted to my parents Najib Fouad Assaf Fayad and Marta Rizk Al Chalouhi and my brothers Fouad Fayad and John Fayad, who have always been a source of unconditional support and encouragement. Their love has provided me with the enthusiasm to face new projects and constantly seek novel challenges.

G.N.F.

To my parents

Najib Fouad Assaf Fayad & Marta Rizk El Chalouhi

and

to my brothers

Fouad Fayad & John Fayad

Contents

List of Figures

List of Tables

Chapter 1

Introduction and background

1.1 Separation of biological molecules using micro/nanofluidic devices

Separation of biological molecules such as DNA and proteins is of great importance for the chemical and pharmaceutical industries [9, 10, 11]. For example, separation of DNA is used for crime investigation [12, 13] and detection and identification of biomarkers in urine [14], while separation of proteins is used for early detection, treatment and prevention of cardiovascular disease [15], and can be similarly applied to lung cancer studies [16].

In recent years, several researchers focused on fabricating regular nanopatterned sieving structures instead of using porous gel media to separate various types of biological molecules. Duong et al. [1] separated long DNA molecules using the one dimensional microfluidic device with a well defined patterned structure shown in Figure 1-1. Their polydimethylsiloxane (PDMS) microstructure allowed short λ-DNA molecules to migrate faster than long T2-DNA. In another study, Volkmuth et al. [2] used microlithography to manufacture a two-dimensional nanostructured array to study the motion of long DNA molecules in a well defined topology as shown in Figure 1-2. Their experimental data shows that they were able to separate DNA molecules up to a length of ~ 100 *kbp*.

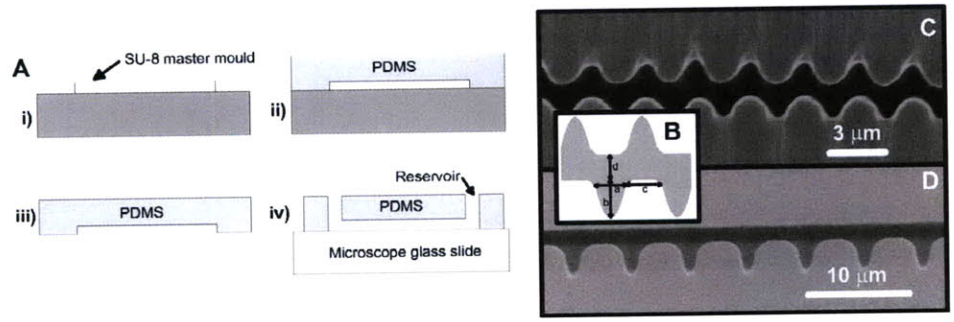

Fig. 1. (A) Process diagram of microchannel fabrication. (i) Convert shaped microchannel mould is fabricated with SU-8. (ii) PDMS is poured and cured over the mould. (iii) PDMS is released from the mould. The microchannel is thus replicated into PDMS. (iv) Reservoirs are punched through PDMS. The microchannel is closed with microscope glass slide. (B) The drawing describes the variables of the periodical cavities (a–d) in the microchannels. The channel width *d* is used to define the channel layouts. (C) SEM top view of moulded 1.5 μm and (D) 3 μm PDMS microchannel.

Figure 1-1: Schematic diagrams and SEM images of the microchannel manufactured by Duong et al. [1]. Adapted from Duong et al. [1].

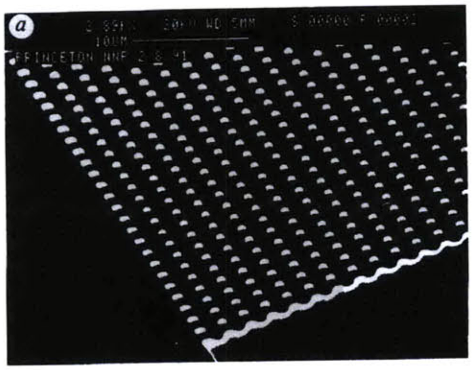

Figure 1-2: Volkmuth's figure shows an electron micrograph of a corner of an array. "The micrograph shows the 0.15 μm-high posts, diameter 1.0 μm, and center to center spacing of 2.0 μm". Adapted from Volkmuth et al. [2].

Fu et al. [3] developed a two-dimensional anisotropic nanofluidic array (see Figure 1-3 from Fu et al. (2007)) to separate short biological molecules. The main reason for this two-dimensional anisotropic sieving structure was to achieve continuous-flow separation. This feature is of great importance for biomarker detection and biosensing with microfluidic systems, since the continuous harvesting of biomolecules of interest would enhance the detection limit for the downstream analysis. The two-dimensional physical landscape of the device can be thought of as a large number of rows of nanofilters separated with deep channels. When biomolecules of different size are injected into the deep channel, they can occasionally jump to the next deep channel through the passage of the nanofilter. The jumping passage rate depends on their size. Hence, molecules will follow different trajectories depending on their size as shown in Figure 1-4.

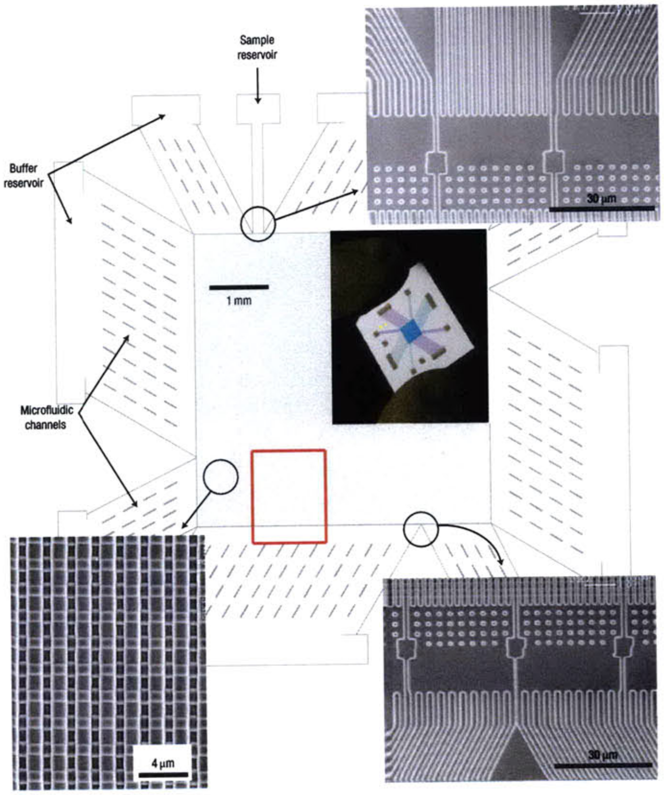

Figure 1-3: "Structure of the microfabricated device incorporating the anisotropic nanofilter array (ANA). Scanning electron microscopy images show details of different device regions (clockwise from top right: sample injection channels, sample collection channels and ANA). The inset shows a photograph of the thumbnail-sized device. The rectangular ANA is $5\ mm \times 5\ mm$. Shallow regions are $1\ \mu m$ wide, $1\ \mu m$ long, $55\ nm$ deep and spaced by $1\ \mu m \times 1\ \mu m$ square silicon pillars. Deep channels are $1\ \mu m$ wide and $300\ nm$ deep. Injection channels connected to the sample reservoir ($1\ mm$ from the ANA top left corner) inject biomolecule samples as a 30-mm-wide stream." Adapted from Fu et al. (2007) [3].

In this Thesis we focus on a specific one-dimenstional device design based on the work of Fu et al. [4] shown in Figure 1-5. This device consists of a large number ($N_p \sim 50,000$) of alternating shallow and deep regions etched in a silicon wafer. Biological molecules (DNA, protein) of contour length L, persistence length L_p and radius of gyration R_g, driven by an electric field through this periodic array of constrictions are

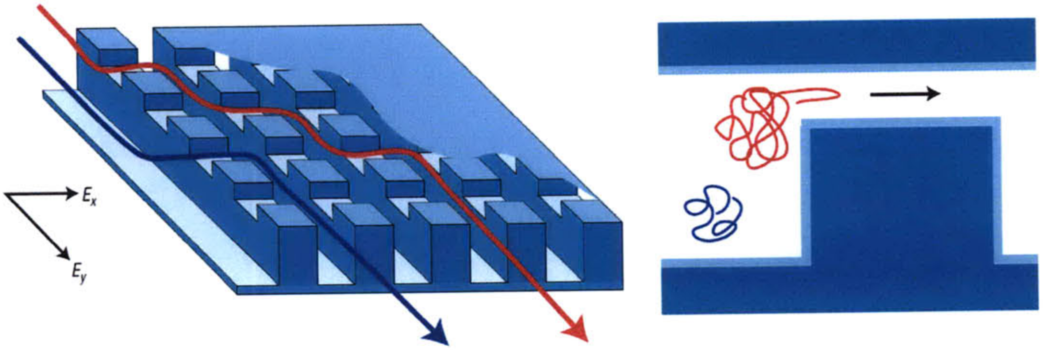

Figure 1-4: Molecules follow different trajectories based on their size. Adapted from Fu et al. (2007) [3].

size-separated because their size-dependent mobilities result in size-dependent travel times. Typical [4] dimensions for the shallow and deep region depths and period are $d_s \approx 55\ nm$, $d_d \approx 300\ nm$ and $p \approx 1\ \mu m$, respectively.

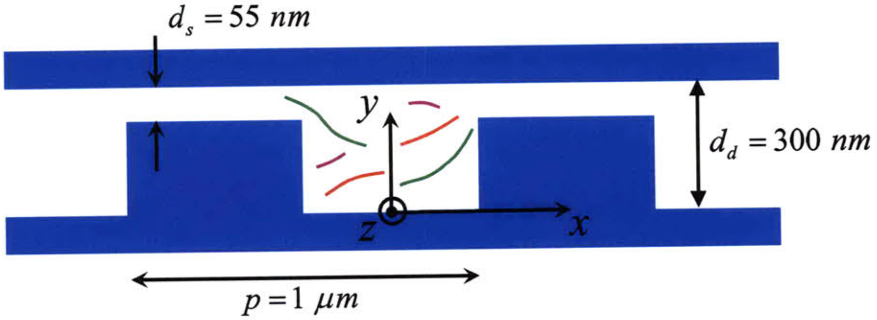

Figure 1-5: Schematic of the nanofilter array.

1.2 Ogston sieving versus entropic trapping

Molecule mobility in these devices is not a monotonic function of molecule length. As Figure 1-6 shows, molecule mobility initially decreases and then increases with molecule length. This leads to two distinct separation regimes: Ogston sieving, where short molecules travel faster than longer molecules and entropic trapping, in which longer molecules travel faster than shorter molecules. Ogston sieving takes place when the molecule radius of gyration is on the order of, or smaller than, the narrow region depth (d_s). In this case, entering the narrow region is a matter of reorientation: short molecules have a larger number of allowable conformations in which they can enter the shallow region in comparison to longer molecules; as a result they spend less time trying to enter the deep region and consequently travel faster in the device (i.e. they will have a higher mobility compared to longer molecules).

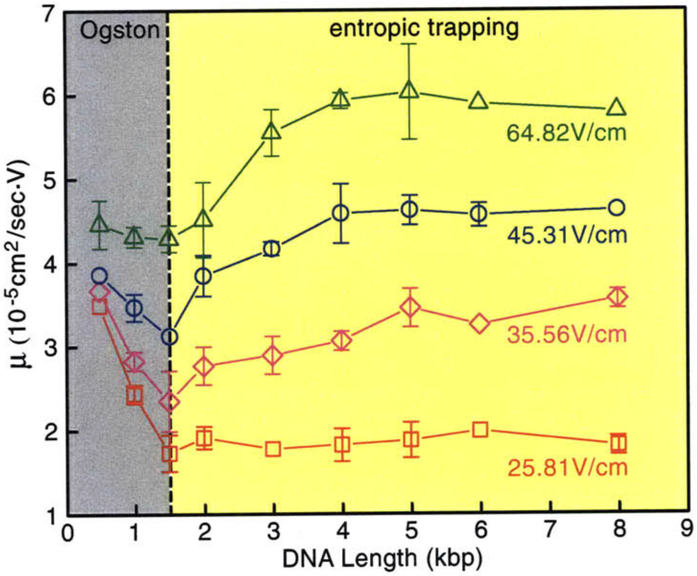

FIG. 3 (color online). Mobility μ as a function of DNA length. DNA fragments were extracted after agarose gel separation. The nanofilter array has $d_s = 73$ nm, $d_d = 325$ nm, $p = 1$ μm. The relative large statistical error bars (drawn if larger than the symbol) are likely due to the low DNA concentrations. The left and right shaded (gray and yellow online) areas indicate Ogston sieving and entropic trapping, respectively. The transition points are marked with the vertical dashed line drawn for DNA length = 1.5 kbp.

Figure 1-6: Ogston entropic transition, adapted from Fu et al. (2006) [4].

Transition to the entropic trapping regime occurs when the molecule radius of gyration is larger than the shallow region depth. In the experimental results of Fu et al. [4] in Figure 1-6, the shallow region depth was $d_s = 73\ nm$. The transition occurs at a DNA length of 540 nm (1500 bp), which has a radius of gyration of $\sim 80\ nm$, as expected.

In the entropic trapping regime, due to their size, the molecules are not freely moving in the device but rather spend most of their time attempting to enter the deep region. While attempting to enter, longer molecules will have longer segments in contact with the shallow region (in the transverse (z) direction), and thus higher probability that some segment of the molecule will enter and pull the remaining part of the molecule. In other words, longer molecules have a higher probability of entering the shallow region and hence have a faster travel velocity in the nanofilter (i.e. they have a higher mobility compared to shorter molecules) [17].

The focus of this Thesis is on Ogston-regime sieving. In particular, we are interested in the separation of short, $L \leq 950$ *bp* (340 *nm*), dsDNA molecules using nanofilter arrays [4, 18] as described previously in Section 1.1. The radius of gyration of the longest DNA molecule (340 *nm*) is 63 *nm* which is close to the shallow region depth $d_s \approx 55$ *nm*.

1.3 Modeling of biological molecule separation

In this Thesis, we focus on the development of a Brownian Dynamics (BD) simulation framework for modeling the performance of nanofluidic separation devices. The ultimate goal of this research is the development of robust simulation methods which can replace costly experimental setups for device design and optimization.

Theoretical modeling of this process is very desirable for gaining fundamental understanding, device optimization and parameter exploration [19, 20, 21]. Despite their small sizes, these devices contain a very large number of solvent molecules making classical molecular dynamics simulations intractable. In other words, for an efficient model, some degree of coarse-graining is required. In this work we show that *for the short molecules* studied here, a Brownian Dynamics (BD) formulation strikes a good balance between fidelity—e.g. agreement with experimental data—and computational efficiency (compared to more expensive coarse-grained techniques such as Dissipative Particle Dynamics [22]). A more complete presentation of our rationale for choosing the Brownian Dynamics method can be found in Section 2.2.

Although BD simulations of biological molecule separation have appeared in the literature before [20, 23], those studies have focused on molecules that are sufficiently longer than L_p, which put the separation mechanism in the entropic trapping regime [4]; moreover, as a result of the significantly larger molecule length, the Brownian Dynamics models were of the freely-jointed bead-spring type. A Brownian Dynamics study of short rod-like molecules in the geometry studied here has appeared recently [19]; however, the focus of that paper was to demonstrate the feasibility of high-field electrophoresis and to highlight the importance of "torque assisted escape" in the latter limit.

The objective of this Thesis is to construct sufficiently realistic and efficient models that can *quantitatively* describe experimental data that are relevant to current engineering practice (low-field). Our models will be guided/validated by the experimental data of Fu et al. [4].

1.4 Brownian Dynamics

Brownian Dynamics [24, 25, 26] is a method for coarse-graining a molecular description of Brownian particles to the mesoscopic level [27]. It corresponds to the simplified version of Langevin Dynamics [28] in the limit where acceleration effects are negligible (overdamped Langevin dynamics). BD formulations achieve considerable computational efficiency gains by treating "explicitly" only the particles of interest; the remaining particles are treated "implicitly" [29] by ignoring the details of their motion and only accounting for their collective effect on the explicit particles, namely, viscous resistance to the latter's motion and random "kicks" modeling the net effect of collisions of the latter with the implicit particles.

As can be expected, such formulations lend themselves naturally to modeling dilute systems of solute particles (e.g. macromolecules) in the presence of a solvent; by focusing only on the solute particles of interest and not solving the equations of motion of the large number of solvent particles, BD formulations enable calculations that would have been out of reach of more traditional ab-initio methods. One of the disadvantages associated with this coarse-graining process is the loss of long-range particle-particle interactions [29]; hydrodynamic interactions may be included in the model [25] at the expense of some algorithmic complexity and computational cost. Using the Chebychev polynomial approximation [30] as originally suggested by Fixman [31], as well as novel schemes for truncating the range of electrostatic and hydrodynamic interactions [32], has resulted in efficient methods that have enabled the practical simulation of long-chain-molecule hydrodynamics in microdevices [33, 32].

1.5 Thesis outline

In Chapter 2, we present a brief discussion of the important dimensional and non-dimensional numbers relevant to the physics of the problem which will help us analyzing the motion of the DNA molecules in the nanofilter. Based on this analysis, we discuss the different numerical approaches that one can choose to tackle the problem of interest.

In Chapter 3, we present the *Worm-Like-Chain* (WLC) BD model [34, 35, 36]. This model includes the effects of bending and stretching stiffness and provides the most accurate description for the DNA molecule. Our implementation of the Worm-Like-Chain model is in line with the work of Allison et al., Hagerman et al., Lewis et al, Klenin et al. [34, 35, 36, 37] and is thus different from Bead-Spring models that are usually used for long molecules [38, 39]. The resulting Brownian Dynamics formulation includes hydrodynamic interactions between beads, and closely models the experimental set up of Fu et al. [4], whose data are used for validation.

In Chapter 4, we present a simpler BD model which treats the DNA molecule as a rigid-rod [40]; this results in significantly reduced computational requirements compared to the WLC model of Chapter 3. On the other hand the model is limited to short rigid rod-like DNA molecules of length $L \lesssim L_p$.

In Chapter 5, we present a further simplified BD model which treats the DNA molecules as non-interacting point particles and accounts for their orientational degrees of freedom through an entropic barrier. The point particle-coefficient-based model we present is based upon the work of [41]. This model is the most efficient and simplest to implement but again is limited to very short, essentially rigid ($L \lesssim L_p$) molecules. The simplicity of this model makes it ideal for applying variance reduction ideas for reducing the statistical uncertainty associated with its predictions.

In Chapter 6, we present a variance reduction methodology for the BD model of Chapter 5. This work extends the original ideas of Baker and Hadjiconstantinou [42, 43] and Al-Mohssen and Hadjiconstantinou [44, 45] who presented variance reduction techniques for solving the Boltzmann equation for low-speed gas flow. Specifically we develop variance reduced BD models based on both formulations used in the above work and show that the formulation of Al-Mohssen and Hadjiconstantinou is more suitable for the applications considered here.

In Chapter 7, we conclude with a summary and an outlook for future research.

Chapter 2

Computational model, dimensional and non-dimensional analysis

2.1 Dimensional and non-dimensional analysis

In this section we review some characteristic physical magnitudes and develop relevant non-dimensional numbers that affect the separation process.

2.1.1 Dimensional analysis

1. **Stokes drag on a bead**

   The drag coefficient on a bead of radius a is given by the Stokes formula

   $$\zeta_{bead} = 6\pi\eta_s a \tag{2.1}$$

   where η_s is the viscosity of the solvent (water), which is taken to be $1.18 \times 10^{-3}\ Pa \cdot s$ following the recent experimental results of Hsieh et al. [46] for the buffer (Tris-Borate-EDTA 5×) used in the experimental setup of Fu et al. [4].

2. **DNA relaxation time**

Polymer relaxation time τ_r can be estimated using Rouse's [47, 48] model:

$$\tau_{r_{Rouse}} = \frac{\zeta_{bead} L^2}{3\pi^2 k_B T} \tag{2.2}$$

or using Zimm's model [48, 49]:

$$\tau_{r_{Zimm}} = \frac{\eta \left(\sqrt{L/L_k} L_k\right)^3}{\sqrt{3\pi} k_B T} \tag{2.3}$$

where k_B is the Boltzmann constant, T is the temperature and $L_k = 2L_p \approx 108\ nm$ is 1 Kuhn length for a dsDNA molecule. Using Equation 2.3 we find that the relaxation time for DNA molecules ranging between $20-340\ nm$ ranges from 9.6×10^{-6} to 6.5×10^{-4} seconds.

3. **Brownian relaxation time**

   Brownian relaxation time is defined by the ratio of the Brownian molecule mass divided by the average drag on the molecule:

$$\tau_B = \frac{\text{Mass}}{\text{Drag}} = \frac{\rho_{\text{DNA}} \pi r_{\text{DNA}}^2 L}{\zeta_{Zimm}} \tag{2.4}$$

where $\rho_{\text{DNA}} = 930\ kg/m^3$ [50] is the DNA density, $r_{\text{DNA}} \sim 1\ nm$ is the DNA geometric radius and ζ_{Zimm} is the drag on the DNA molecule as predicted by Zimm's model [49, 48] given by:

$$\zeta_{Zimm} = \frac{3\sqrt{6\pi^3}}{8} \eta_s \sqrt{L L_k} \tag{2.5}$$

The Brownian relaxation time ranges from 10^{-13} to 10^{-12} seconds for DNA of length 20 to 340 nm. The smallest timescale we are interested in simulating is on the order of:

$$t_s \sim \frac{d_s^2}{D} \sim \frac{d_s^2\, \zeta_{Zimm_{(20\,nm)}}}{k_B T} \sim 10^{-4}\,\text{seconds} \tag{2.6}$$

where d_s is the smallest geometric dimension in the device of interest and D is the largest diffusion coefficient which corresponds to the smallest DNA molecule of interest (20 *nm*). We estimate the largest diffusion coefficient using the Zimm model [49] which agrees very well with the experimental measurements [51]. Since the smallest timescale we are interested in simulating is much larger than τ_B, this means that our system is highly damped and we can neglect inertia in our simulations.

4. **Radius of gyration**

   The mean square radius of gyration of the Worm-Like-Chain Kratky-Porod model was first calculated by Benoit and Doty [52] and is given by:

$$\langle R_g^2 \rangle = \frac{1}{3} L_p L - L_p^2 + 2\frac{L_p^3}{L} - 2\frac{L_p^4}{L^2}\left(1 - \exp\left(-\frac{L}{L_p}\right)\right) \tag{2.7}$$

   For the experimental data of Fu et al. [4] the radius of gyration of the longest DNA molecule (270 *nm*) is 53.6 *nm* which is almost equal to the shallow region depth. This places the separation process in the Ogston regime (where the primary sieving mechanism derives from the steric hindrance due to the restriction) or the early transition region between the Ogston regime and entropic trapping [4].

5. **Root mean square end-to-end distance**

   The mean square end-to-end distance of a flexible molecule as predicted by the Kratky-Porod model [5, 6] is given by:

$$\langle L_{ee}^2 \rangle = 2LL_p \left[1 - \frac{L_p}{L}\left(1 - \exp\left(-\frac{L}{L_p}\right)\right)\right] \tag{2.8}$$

   In our study the dsDNA persistence length was about 54 *nm*. For a 54 *nm* DNA molecule, the Kratky-Porod model (Equation 2.8) predicts about 17% difference between the contour length and the root mean square end-to-end distance of the molecule (see Figure 2-1). In other words a rigid-rod-like model is expected to be a reasonable model for molecules up to 54 *nm* (150 *bp*) in length. Since in this Thesis we study molecules with length up to 340 *nm*

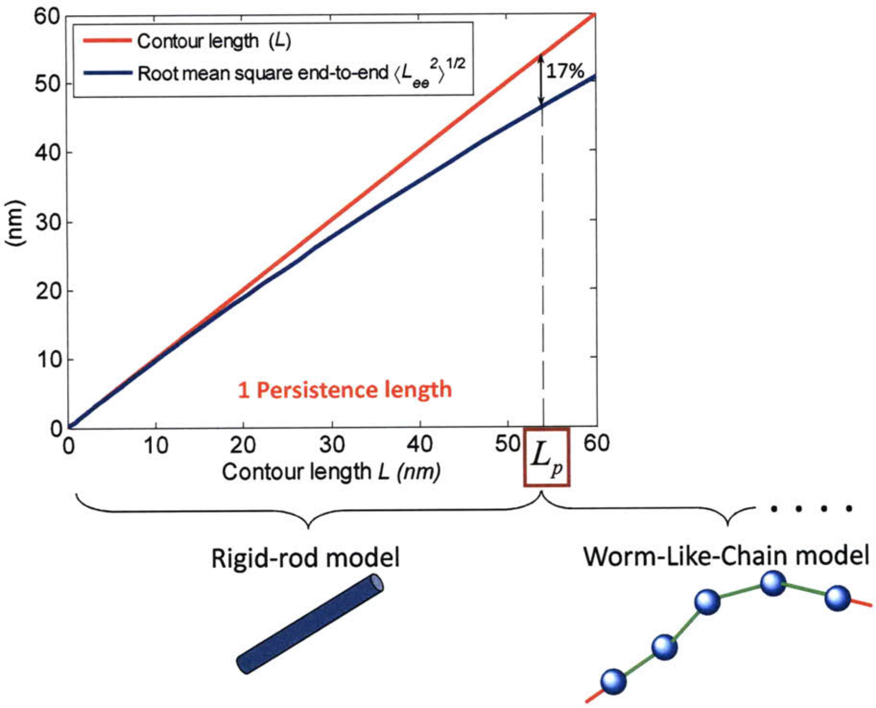

Figure 2-1: Root mean square end-to-end distance versus contour length using Kratky-Porod model [5, 6].

(950 *bp*) a Worm-Like-Chain model, which takes DNA backbone flexibility into account, is used.

2.1.2 Non-dimensional analysis

1. **Translational Péclet number**

   The translational Péclet number Pe_t compares the importance of advection relative to diffusion. In this nanofluidic device, the translational Péclet number can be defined as

$$Pe_t = \frac{\mu E_{av} p}{D} = \frac{q' L E_{av} p}{k_B T} \tag{2.9}$$

   where $\mu \approx 6.3 \times 10^{-5}\ cm^2/Vs$ is the free solution mobility, E_{av} is the applied electric field, $p \sim 1000\ nm$ is the device pitch length which is the characteristic distance over which advection and diffusion rates are compared, D is the molecule diffusion coefficient and q' is the DNA effective charge per unit length discussed in detail in section 3.7.1. In the experimental setup of Fu et al. [4] the minimum and maximum translational Péclet numbers are as follows:

- **Minimum translational Péclet number** $Pe_{t_{min}} \sim 0.25$ corresponds for the case where $E_{av} = 10\ V/cm$ and $L_{\text{DNA}} = 18\ nm$ (shortest DNA molecule used in the experiments). Such molecule has a diffusion coefficient $D_{18\ nm} \approx 25\ \mu m^2/s$.
- **Maximum translational Péclet number** $Pe_{t_{max}} \sim 11.5$ corresponds for the case where $E_{av} = 64\ V/cm$ and $L_{\text{DNA}} = 270\ nm$ (longest DNA molecule used in the experiments). Such molecule has a diffusion coefficient $D_{270\ nm} \approx 3.5\ \mu m^2/s$.

2. **Rotational Péclet number**

   The relative effects of rotation due to the electric field gradient and rotational diffusion are quantified by the rotational Péclet number Pe_r [19] given by:

$$Pe_r = \left(\frac{1-\epsilon^2}{\nu+\epsilon}\right)\left(\frac{q' E_{av} L^2}{12 k_B T}\right) \tag{2.10}$$

   where $\epsilon = d_s/d_d$ is the ratio of the shallow region depth $d_s \sim 55\ nm$ to the deep region depth $d_d \sim 300\ nm$, ν is the length ratio between the shallow and deep region. The maximum rotational Péclet number ~ 0.04 corresponds to the longest DNA molecule ($L = 108\ nm$) for which we assume a rigid-rod-like model – see Chapter 4 for details – along with the highest electric field $E_{av} = 64\ V/cm$.

3. **Reynolds number**

   Reynolds number measures the ratio of inertial forces to viscous forces. Reynolds number based on the molecule contour length $Re_{L_{\text{DNA}}}$ is given by

$$Re_{L_{\text{DNA}}} = \frac{V_{\text{DNA}} L}{\nu_s} = \frac{\rho \mu E L_{\text{DNA}}}{\eta_s} \tag{2.11}$$

   where $\nu_s = \eta_s/\rho = 1.18 \times 10^{-6} m^2/s$ is the fluid (water in our case) kinematic viscosity, μ is the free-solution mobility. The maximum Reynolds number in the experimental setup is 10^{-5}.

2.1.3 Summary

We summarize all these dimensional and non-dimensional numbers in Table 2.1 and Table 2.2, respectively. Note that the minimum and maximum values do not necessarily correspond to the shortest and longest DNA molecule.

		Minimum	Maximum
DNA Length	L	18 nm (50 bp)	340 nm (950 bp)
DNA relaxation time	τ_r	9.6×10^{-6} (s)	6.5×10^{-4} (s)
Brownian relaxation time	τ_B	10^{-13} (s)	10^{-12} (s)
Radius of gyration	R_g	–	63.1 (nm)
Root mean square end-to-end distance	$\langle L_{ee}^2 \rangle^{1/2}$	17.1 (nm)	175.8 (nm)

Table 2.1: Summary of dimensional values of key physical parameters.

		Minimum	Maximum
Translational Péclet number	Pe_t	0.25	11.5
Rotational Péclet number	Pe_r	3.7×10^{-4}	4×10^{-2}
Reynolds number	Re_L	10^{-7}	10^{-5}

Table 2.2: Summary of the dimensionless numbers.

From these values we can draw the following conclusions which will be used throughout our modeling efforts:

1. The separation process falls into the Ogston sieving regime
2. Particle inertia can be neglected since we are in a highly damped system.
3. The translational diffusion and advection effects are both equally important since the translational Péclet number is $\sim O(1)$.
4. The rotational diffusion is dominant in comparison to rotational torque due to electric field gradient since the rotational Péclet number is very small ($Pe_r <$

$0.05 \ll 1$). This will help us develop a simple partition-coefficient-based model in Chapter 5.

5. Inertial forces are negligible compared to viscous forces and drag forces will be estimated using Stokes law [53].

2.2 Why Brownian Dynamics ?

Efficient simulations of DNA separation are difficult to achieve due to the multi-scale and multi-physics nature of the problem. Specifically, although microscopic in nature, the device dimensions are sufficiently large, and the separation timescale sufficiently long (seconds), to make Molecular Dynamics (MD) [24] simulations intractable. On the other hand, a continuum approach, e.g. through computational fluid dynamics (CFD) [54], places insufficient emphasis on the dominant physics of interest. Specifically, a CFD approach focuses exclusively on a detailed hydrodynamic description while neglecting Brownian (entropic) effects. Although addition of Brownian fluctuations to continuum (Navier-Stokes) formulations has been investigated [55], previous work has been limited to simple systems and does not extend easily to the macromolecules of interest here. Moreover, the computational complexity associated with CFD approaches including rigid (rod) or semi-rigid (Worm-Like-Chain) moving objects in the computational domain makes these methods not preferable in view of the above limitations.

For the above reasons, mesoscopic approaches have attracted some interest. Dissipative Particle Dynamics (DPD) [56] has attracted interest due to its ability to naturally capture thermal fluctuations and the DNA particulate nature. DPD reduces computational cost (compared to MD) by coarse-graining length and timescales by "lumping" many actual molecules into computational particles that obey appropriately modified equations of motion. Unfortunately, this technique is too computationally expensive for our application since the coarse-graining is limited by the need to capture details at the level of the shallow region depth $d_s \sim 55\ nm$. In other words, the computational cost of DPD will be very close to that of MD for the systems of interest to this Thesis. We also mention the Lattice Boltzmann method [57] which may be useful as a qualitative simulation tool.

Given the above considerations we have decided to use a Brownian Dynamics (BD) [38, 26, 40, 34, 25] approach. As explained in Section 1.4, in BD only the equations of motion of the molecules of interest (here, DNA) are solved, while the solvent is modeled as a continuum medium interacting with the molecule of interest through random (Brownian) and deterministic (drag) forces.

In this Thesis we explore BD models of varying degrees of coarse-graining in search of computational efficiency while retaining satisfactory agreement with the experimental data of Fu et al. [4]. Specifically, we present three Brownian Dynamics models:

1. Flexible Worm-Like-Chain (WLC) model discussed in detail in Chapter 3.
2. Rigid rod-like model discussed in detail in Chapter 4.
3. Point-particle partition-coefficient-based model discussed in detail in Chapter 5.

Chapter 3

Flexible Worm-Like-Chain (WLC) model

3.1 Introduction

In this Chapter we focus on the development of a Brownian Dynamics [26, 38, 34] simulation framework for modeling the performance of the nanofluidic separation devices discussed in Chapter 1. This work utilizes the Worm-Like-Chain (WLC) model [34, 35, 36] which includes the effects of bending and stretching stiffness. Our implementation of the Worm-Like-Chain model is in line with the work of Allison et al., Hagerman et al., Lewis et al, Klenin et al. [34, 35, 36, 37] and is thus different from Bead-Spring models that are usually used for long molecules [38, 39].

The resulting Brownian Dynamics formulation includes hydrodynamic interactions between beads, and closely models the experimental set up of Fu et al. [4], whose data are used for validation. The material presented here has appeared in a more condensed form in [58].

3.2 The WLC model

In typical WLC treatments [34], the molecule is modeled as an elastic chain consisting of N beads of radius a connected by $N-1$ elastic links of average length L_0 as shown in Figure 3-1. In the present work we use a slightly modified discretization which

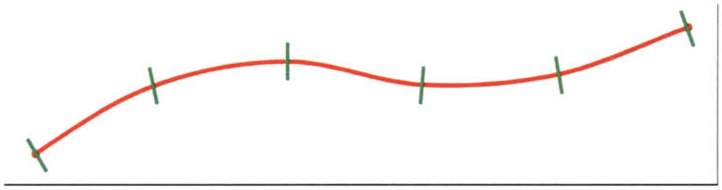

(a) DNA molecule divided into N segments.

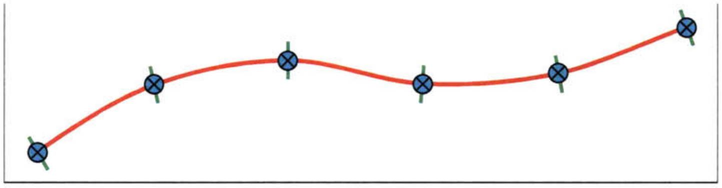

(b) Beads located at the ends of each segment.

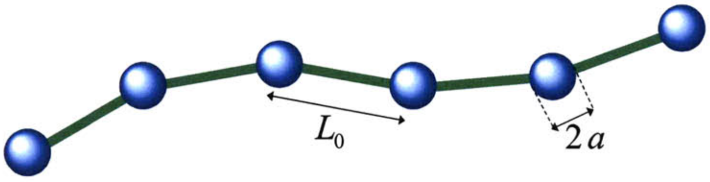

(c) DNA molecule discritized into $N-1$ links and N beads.

Figure 3-1: DNA descretization into $N-1$ links and N beads.

features N beads and N segments, as shown in Figure 3-2. In this discretization, each bead represents the same fraction of chain length and hence makes the application of a common bead size and effective charge more justified. The beads are connected by $N-1$ elastic links (shown in green in Figure 3-2). The half segments on each end of the molecule are assumed to be an extension of their nearest link, and are used in defining the molecule shape, e.g. during boundary condition imposition. Our numerical formulation otherwise follows the work of Klenin et al. [34]; the chain elasticity includes stretching and bending contributions.

Our chain conformation is specified by the locations $\mathbf{r}_i$, $i = 1, \ldots, N$ of the N beads comprising the chain and which are located at the vertices of the $N-1$ straight links. The links are represented by the vectors $\mathbf{s}_i = \mathbf{r}_{i+1} - \mathbf{r}_i$, $i = 1, \ldots, N-1$; we define $s_i = |\mathbf{s}_i|$ as the magnitude of the vector $\mathbf{s}_i$; in addition the unit vector along each link is defined by $\mathbf{e}_i = \mathbf{s}_i / s_i$ (see Figure 3-3).

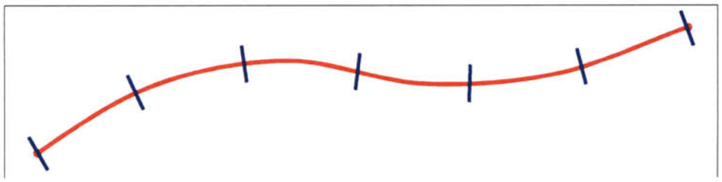

(a) DNA molecule divided into N segments.

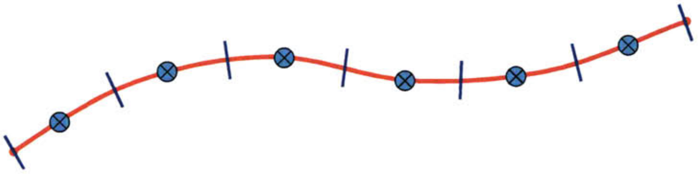

(b) Beads located at the middle of each segment.

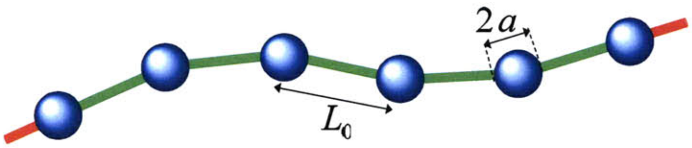

(c) Beads are connected by $N-1$ elastic links.

Figure 3-2: DNA molecule divided into N segments, N beads and $N-1$ connecting links.

3.3 Equations of motion

The governing equations for the system of these N beads are Langevin-type equations of motion:

$$m_i\ddot{\mathbf{r}}_i = -\sum_{j=1}^{j=N} \zeta_{ij}\dot{\mathbf{r}}_j + \mathbf{F}_i^{(systematic)} + \mathbf{F}_i^{(random)} \quad , \quad i = 1, \ldots, N \tag{3.1}$$

where the change in momenta $m_i\ddot{\mathbf{r}}_i$ is balanced by the sum of all the external forces applied on bead i. The drag force exerted by the surrounding fluid is accounted for by $-\sum_{j=1}^{j=N} \zeta_{ij}\dot{\mathbf{r}}_j$, while $\mathbf{F}_i^{(systematic)}$ is a systematic force due to the interaction between the beads due to the stretching and bending forces between the beads as well as the external electric field force. Finally, $\mathbf{F}_i^{(random)}$ represents randomly fluctuating forces exerted on each bead by the surrounding fluid. The systematic forces are discussed in more detail below.

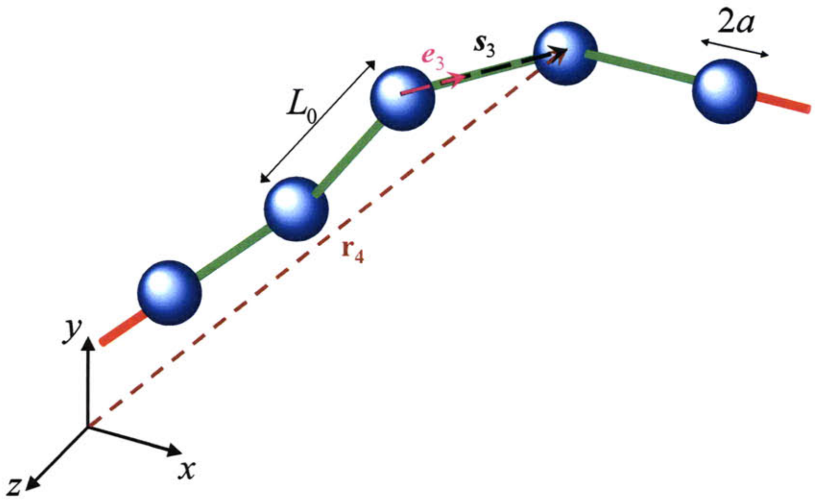

Figure 3-3: WLC beads positions.

3.3.1 Systematic forces

The systematic forces mentioned above can be divided into the stretching and bending forces between beads, in addition to the external electric field force. In order to calculate the stretching and bending forces we start by calculating their respective stretching and bending energies.

3.3.1.1 Stretching force

Following Klenin et al. [34], we define the stretching energy for each segment i as

$$\frac{E_i^{(stretching)}}{k_B T} = \frac{(L_0 - s_i)^2}{2\,(L_0\delta)^2} \tag{3.2}$$

where k_B is the Boltzmann constant, T is the temperature, L_0 is the link equilibrium length and δ is the stiffness parameter chosen such that $(L_0\delta)^2$ is approximately equal to the variance of the link length distribution.

Hence the stretching force on the ith vertex from the $(i+1)$th one is parallel to the ith link and is given by:

$$\frac{\mathbf{F}_{i,next}^{(stretching)}}{k_B T} = \frac{(s_i - L_0)}{(L_0\delta)^2}\mathbf{e}_i \tag{3.3}$$

Finally, the total stretching force on the ith vertex is

$$\mathbf{F}_i^{(stretching)} = -\mathbf{F}_{i-1,next}^{(stretching)} + \mathbf{F}_{i,next}^{(stretching)} \tag{3.4}$$

3.3.1.2 Bending force

Similarly, we start by defining the bending energy for the ith joint as:

$$\frac{E_i^{(bending)}}{k_B T} = \alpha_{bending}\beta_i^2 \tag{3.5}$$

where β_i is the angle between $\mathbf{s}_{i-1}$ and $\mathbf{s}_i$; $\alpha_{bending}$ is the bending rigidity parameter chosen in such a way that the mean-square end-to-end distance of the dsDNA molecule equals that predicted by the Kratky-Porod [5, 6] model

$$\left\langle L_{ee}^2 \right\rangle = 2L_p L \left[1 - \frac{L_p}{L}\left(1 - e^{-L/L_p}\right)\right] \tag{3.6}$$

Here the dsDNA persistence length was taken to be $L_p = 54\ nm$ [4, 59].

The bending force is calculated from the bending energy. The bending force acting on the ith vertex from the $(i+1)$th one is perpendicular to the ith segment and lies in the bend plane. It is given by

$$\frac{\mathbf{F}_{i,next}^{(bending)}}{k_B T} = \frac{2\alpha_{bending}\beta_i}{s_i}\tilde{\mathbf{p}}_{\mathrm{i}} \times \mathbf{e}_i \tag{3.7}$$

where $\tilde{\mathbf{p}}_i = (\mathbf{e}_{i-1} \times \mathbf{e}_i) / \sin\beta_i$. Similarly, the contribution of the bending force acting on the ith vertex from the $(i-1)$th vertex is perpendicular to the $(i-1)$th segment and also lies in the bend plane. It is given by

$$\frac{\mathbf{F}_{i,prev}^{(bending)}}{k_B T} = \frac{2\alpha_{bending}\beta_i}{s_{i-1}}\tilde{\mathbf{p}}_{\mathrm{i}} \times \mathbf{e}_{i-1} \tag{3.8}$$

Finally, the total bending force for the ith vertex is

$$\mathbf{F}_i^{(bending)} = -\mathbf{F}_{i-1,next}^{(bending)} + \mathbf{F}_{i,prev}^{(bending)} + \mathbf{F}_{i,next}^{(bending)} - \mathbf{F}_{i+1,prev}^{(bending)} \tag{3.9}$$

3.3.1.3 Electric field force

The electric field force assigned to each bead is calculated using the following equation:

$$\mathbf{F}_i^{(Electric)} = q_{bead} E|_{\mathbf{r}_i} \tag{3.10}$$

where q_{bead} is the effective charge on each bead. The latter is equal to the effective charge of the DNA molecule (see Section 3.7.1) divided by the total number of beads. $E|_{\mathbf{r}_i}$ is the value of the electric field at the position ($\mathbf{r}_i$) of the bead.

The electrostatic force is calculated based on the bead effective charge and the electric field due to the externally applied voltage difference across the device (ΔV). The electric field is pre-computed on a triangular grid with maximum edge size of approximately 2 nm assuming insulating boundary conditions at the walls using the MATLAB *Partial Differential Equation Toolbox.* An approximation to this solution is stored on a square grid for quick access; each square has a side of 5 nm. The piecewise constant electric field value associated with every square is the average value over all triangle centroids within the square. Note that due to the extremely fine initial triangular grid (more than 10^5 elements) and the very fine square "interpolation" grid (more than 10000 squares) the error associated with this approximation is negligible compared to the modeling approximations and experimental uncertainties involved.

3.4 Numerical integration algorithm

The equation of motion [34, 25] of each bead is integrated using the two-step algorithm of Klenin et al. [34]. In the first step we calculate a "predicted" displacement using

$$\mathbf{r}_i'(t + \Delta t) = \mathbf{r}_i(t) + \sum_{j=1}^{N} \mathbf{D}_{ij}(t) \frac{\mathbf{F}_j(t)}{k_B T} \Delta t + \mathbf{R}_i \quad , \quad i = 1, \ldots, N \tag{3.11}$$

where Δt is the time step and $\mathbf{F}_j(t)$ denotes the force on bead j; this force includes contributions from the externally applied electric field (Section 3.3.1.3), as well as intra-bead forces discussed in Section 3.3.1. Here $\mathbf{D}_{ij}(t)$ denotes the diffusion interaction tensor between beads i and j, which accounts for hydrodynamic interactions between these two beads; this is further discussed in Section 3.5. Finally, k_B is Boltzmann's constant and T is the simulation temperature. As implied by the notation, $\mathbf{D}_{ij}(t)$ and $\mathbf{F}_j(t)$ are calculated from the conformation $\{\mathbf{r}_i(t),\ i = 1, \ldots, N\}$ corresponding to time t.

The random displacements $\mathbf{R}_i$ are defined by

$$\langle \mathbf{R}_i \rangle = 0 \tag{3.12}$$

$$\langle \mathbf{R}_i \otimes \mathbf{R}_j \rangle = 2\mathbf{D}_{ij}\Delta t \tag{3.13}$$

and can be calculated from a weighted sum of normal random deviates [34, 25]. Following the recommendation of Klenin et al., the diffusion tensor is updated every 10 time steps thus reducing the number of times the expensive factorization needs to be performed.

Finally, the second integration step is

$$\mathbf{r}_i(t + \Delta t) = \mathbf{r}_i^{'}(t + \Delta t) + \sum_{j=1}^{N} \mathbf{D}_{ij}(t) \frac{\mathbf{F}_j^{'}(t + \Delta t) - \mathbf{F}_j(t)}{k_B T} \Delta t \quad , \quad i = 1, \ldots, N \tag{3.14}$$

where $\mathbf{F}_j^{'}(t + \Delta t)$ are the forces calculated from the conformation $\{\mathbf{r}_i^{'}(t + \Delta t),\ i = 1, \ldots, N\}$.

3.5 Hydrodynamic interactions

Hydrodynamic interactions between the beads are accounted for using the Rotne-Prager tensor [60]:

$$
\begin{aligned}
\mathbf{D}_{ij} &= D_0 \mathbf{I} && if \quad i = j \\
\mathbf{D}_{ij} &= D_0 \frac{3a}{4r_{ij}} \left[\mathbf{I} + \frac{\mathbf{r}_{ij} \otimes \mathbf{r}_{ij}}{r_{ij}^2} + \frac{2a^2}{3r_{ij}^2} \left(\mathbf{I} - 3\frac{\mathbf{r}_{ij} \otimes \mathbf{r}_{ij}}{r_{ij}^2} \right) \right] && if \quad r_{ij} \geq 2a, \quad i \neq j \\
\mathbf{D}_{ij} &= D_0 \left[\left(1 - \frac{9}{32} \frac{r_{ij}}{a} \right) \mathbf{I} + \frac{3}{32} \frac{\mathbf{r}_{ij} \otimes \mathbf{r}_{ij}}{a r_{ij}} \right] && if \quad r_{ij} \leq 2a, \quad i \neq j
\end{aligned}
\tag{3.15}
$$

where $D_0 = k_B T / 6\pi\eta_s a$, η_s is the solvent viscosity, $\mathbf{r}_{ij} = \mathbf{r}_j - \mathbf{r}_i$, $r_{ij} = |\mathbf{r}_{ij}|$, $\mathbf{I}$ is the unity tensor, and $\mathbf{r} \otimes \mathbf{r}$ denotes the dyadic product.

The bead radius is chosen such that a reference DNA chain—a chain of contour length equal to one persistence length—has the desired diffusion coefficient. This is further discussed in Section 3.7.

3.6 Boundary conditions

Interactions with the walls are steric; in other words, if during a move, part of the molecule extends beyond one of the system boundaries, the move is rejected. In such a case, the molecule is assigned its original position, and a new step is taken which is again checked for boundary crossing. We have considered both including and neglecting the time increment during rejected moves; the difference to our results is negligible due to the small time step used which results in a number of rejected steps that is less than 1% of the total number of steps. Several researchers [23, 19] have used similar boundary conditions. Reflecting boundary conditions, whereby a molecule (or parts of a molecule) is returned to the domain by taking the mirror image of the "offending" move, have also been used in some studies [21].

3.7 Simulation parameters

In accordance with the experiments of Fu et al. [4], we consider dsDNA molecules of lengths $18\ nm \leq L \leq 324\ nm$ in a Tris-Borate-EDTA $5\times$ buffer which diminishes the effect of electro-osmotic flow [61]. We consider average electric fields $E_{av} = \Delta V/(pN_p)$ in the range $20 - 400\ V/cm$. The viscosity of the solvent (water) is taken to be $1.18 \times 10^{-3}\ Pa \cdot s$ following the recent experimental results of Hsieh et al. [46] for the buffer considered here.

The timestep was $10^{-8}\ s$. This value was chosen such that all guidelines set by Klenin et al. [34] are satisfied. The total simulated time modeling the experiments of Fu et al. varied between 15 and 60 minutes (depending on the molecule length and electric field), and was such that the molecule traverses at least $10,000$ periods. We have also verified that the initial position and configuration of the DNA molecule does not affect our results. In fact, to make sure that no "initial condition" effects are present, we start collecting data on the distance traveled by the molecule after 10^8 timesteps of relaxation (no field) and 10^8 timesteps of motion under the action of the electric field. The statistical uncertainty in the majority of our calculations is less than 1%, leading to error bars that are smaller than the symbols on the graph. Error bars are given when the statistical uncertainty is sufficiently large for the error bars to be visible.

Although it would have been desirable to use the same discretization (e.g. same discretization length L_0) for all molecules studied here, the range of lengths studied makes this impractical. In the interest of computational efficiency, the degree of coarse-graining increases in three steps: for $20.25\ nm \leq L \leq 54\ nm$ we use $L_0 = 6.75\ nm$; for $54\ nm \leq L \leq 108\ nm$ we use $L_0 = 13.5\ nm$; for $108\ nm \leq L \leq 324\ nm$ we use $L_0 = 27\ nm$. Our simulation method becomes inefficient for significantly longer molecules, primarily due to the hydrodynamic interactions.

In view of the above steps in discretization, special attention was paid to ensure that the molecule drag (and diffusion coefficient) remains a smooth and continuous function of the molecule length. This was achieved (see Figure 3-4) by using a different bead diameter for different discretizations. Given that the bead size remains constant for the same discretization, fixing the bead size for one "reference" molecule uniquely determines the bead size of all molecules. Here, the bead size of the reference dsDNA molecule ($L = 54\ nm, L_0 = 13.5\ nm$) was chosen such that the simulated diffusion coefficient $\hat{D}(L = 54\ nm)$ of this molecule in water (viscosity $1 \times 10^{-3}\ Pa \cdot s$) matches the corresponding experimental result of Lukacs et al. [7] who performed experiments for short dsDNA ($7\ nm < L < 2040\ nm$) diffusing in water.

Using this procedure, our simulations yield a diffusion coefficient $\hat{D}(L)$ which is in excellent agreement with the experimental data as can be seen in Figure 3-4. In fact, for molecules longer than 80 nm the resulting diffusion coefficient varies as $L^{-0.71}$, in excellent agreement with the exponent of Lukacs et al. [7] (-0.72).

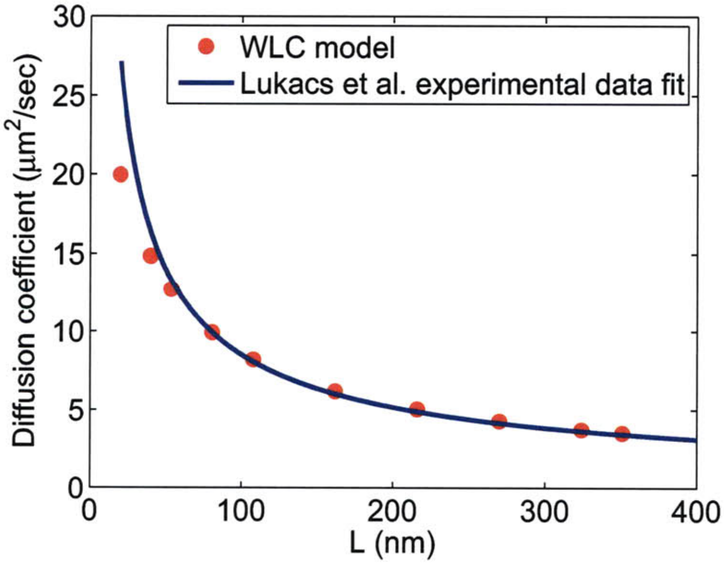

Figure 3-4: Comparison between our simulation results and the experimental data of Lukacs et al. [7] for the diffusion coefficient of dsDNA molecules in water.

3.7.1 Modeling the free-draining mobility

Assuming a constant charge per unit length, q', the Nerst-Einstein relation

$$\frac{\hat{D}}{\mu_{NE}} = \frac{k_B T}{q' L} \tag{3.16}$$

predicts that the Nerst-Einstein mobility scales with the molecule length according to $\mu_{NE} \propto L^{0.29}$.

However, as discussed extensively in the literature [62, 63, 64, 51], in the presence of electric forces, hydrodynamic screening results in a free-solution mobility that is, to a very good approximation, independent of the dsDNA length (and different from the theoretically predicted μ_{NE}). This free-solution mobility will be denoted here by μ_{fs}.

Of particular interest are the careful experiments of Nkodo et al. [51] which clearly show that while μ_{fs} is independent of the molecule length, the molecule diffusivity is unaffected by the electric field, exhibiting Zimm scaling for sufficiently long molecules (Nkodo et al. report an exponent ranging between -0.68 and -0.86 for short ssDNA molecules; this compares well with the value of -0.72 of Lukacs et al. and -0.71 found here for dsDNA molecules).

Developing a Brownian Dynamics model which captures these phenomena from first principles is very difficult. On the other hand, neglecting hydrodynamic interactions as in previous studies will result in a molecule diffusivity that scales as L^{-1}, which differs significantly from the expected behavior. This is particularly important in the present work where the experimental translational Péclet number $Pe_t = q' L E_{av} p / k_B T$ ranges between 0.25 and 11.5, requiring accurate representation of the balance between diffusion and advection. As we show below, a nonlinear response to the electric field appears for $Pe_t \gtrsim 3.6$ for the device designed and tested by Fu et al. [4].

To circumvent these difficulties we implemented a method which allows the free-draining behavior to be reproduced with minimal modification to the BD algorithm, and virtually no effect on the diffusion coefficient. The method amounts to allowing the molecule effective charge per unit length to vary with L such that the observed (free-draining) mobility is independent of the molecule length. In other words we let

$$q'(L) = (L/L_p)^{-0.29} q'_{ref} \tag{3.17}$$

such that

$$\mu_{fs} = \frac{q' L \hat{D}}{k_B T} \tag{3.18}$$

is independent of L. Note that because the variation of q' with L is dictated by the experimental data [51, 65] the only adjustable parameter in the model is the value of q'_{ref} which, due to the choice $q'(L = 54\ nm) = q'_{ref}$, can be thought of as the effective charge of the reference molecule; the value used for q'_{ref} in this work will be given in the next section. Moreover, due to its relatively weak dependence on L, q' varies by less than a factor of 3 over the range $20.25\ nm \leq L \leq 324\ nm$ studied here.

3.8 Simulation results

Our simulations suggest that the device geometry affects molecule transport significantly. For this reason, we have modeled the following two geometries:

1. Square-well geometry (Figure 1-5) with dimensions $d_s = 55\ nm$, $d_d = 300\ nm, p = 1\ \mu m$ as given in [4].
2. Tapered geometry shown in Figure 3-5. The shape of the transition from deep to shallow regions was transcribed from the SEM image of a similar device ($p = 2\ \mu m$) shown in [4]. The resulting model geometry is characterized by $d_s = 55\ nm$, $d_d = 300\ nm, p = 1\ \mu m$, and a taper angle of 62°; the transition from the deep to the narrow region occurs in 2 steps as shown in Figure 3-5.

These two geometries result in substantially different mobility levels (about 40%). For this reason, for each geometry the value of q'_{ref} was chosen such that the resulting

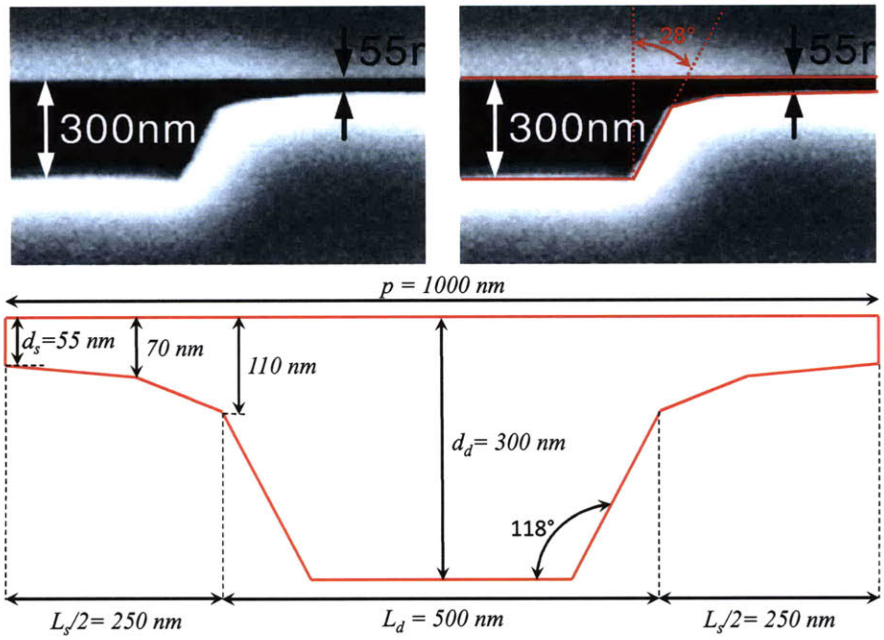

Figure 3-5: SEM image and more realistic geometry.

mobility is in agreement with one reference experimental result ($L = 20.25\ nm$, $E = 64.3\ V/cm$). The resulting values of q'_{ref} are $5.9 \times 10^{-11} \frac{C}{m}$ for case 1 and $4.3 \times 10^{-11} \frac{C}{m}$ for case 2. The value of effective charge, especially for the more realistic case 2, compares very favorably with the value given by Smith et al. [66] ($4.45 \times 10^{-11} \frac{C}{m}$) Figure 3-6 shows a comparison between our simulation results for the two geometries shown in Figure 1-5 and 3-5 and the experimental results of Fu et al. In addition to a significantly different mobility level, our model shows that the two geometries result in different molecule selectivity. Although the tapered geometry results in inferior selectivity, not surprisingly, it is in better *overall* agreement with the experimental results of Fu et al., compared to the idealized geometry. Our results also show that for the realistic geometry of Figure 3-6(b) , the molecule mobility increases non-linearly with increasing electric field for $Pe_t \gtrsim 3.6$.

3.8.1 Molecular Probability Distribution

Although the Brownian Dynamics method is inherently stochastic and yields noisy results, characterization of the complete molecule probability distribution is feasible

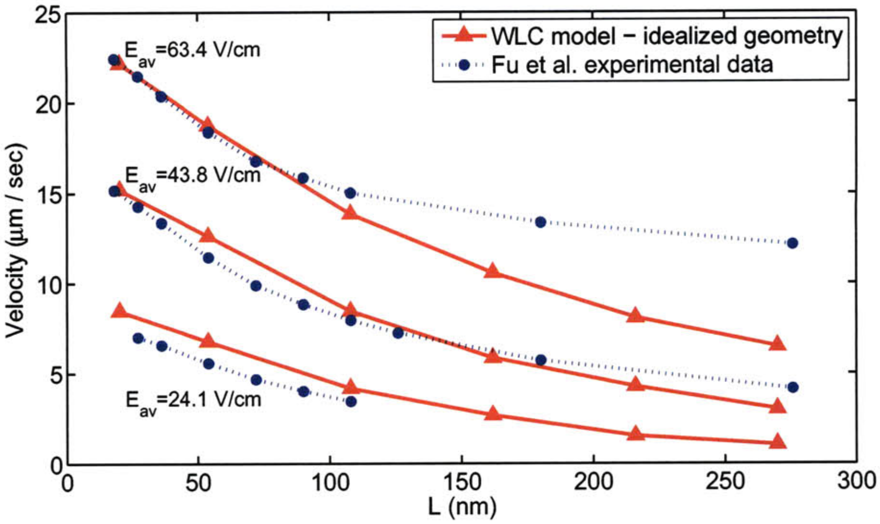

(a) Comparison with experimental results for the idealized geometry of Figure 1-5.

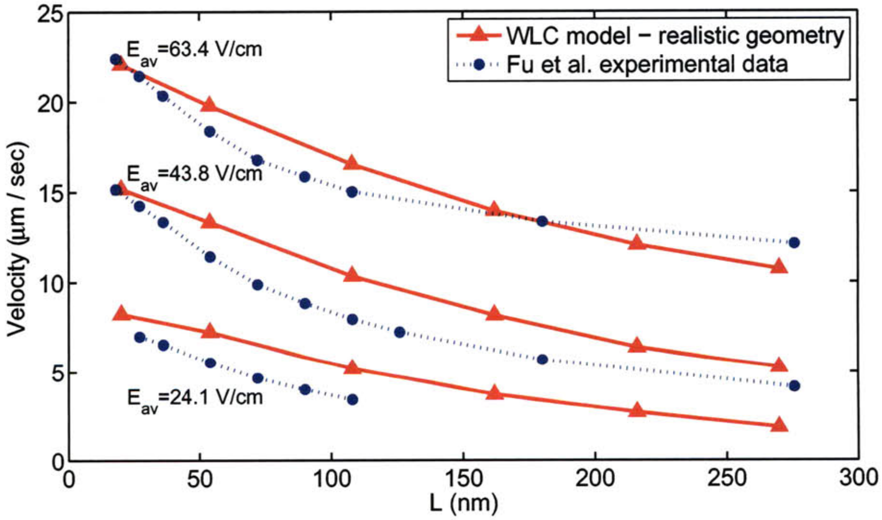

(b) Comparison with experimental results for the more realistic geometry of Figure 3-5.

Figure 3-6: WLC model simulation results for different geometries.

and not very computationally intensive. The plots shown here are obtained by discretizing the simulation domain into small cells and recording the relative frequency of occupation by the mid-point of the molecule. These results are plotted in the figure as two-dimensional contour plots as well as one-dimensional density plots as a function of the device length; the latter are obtained by integrating the two-dimensional density in the direction normal to the direction of travel. These plots can be very useful for obtaining a qualitative understanding of the device operation. For example, the comparison of Figures 3-7 and 3-8 can be used to investigate the origin of the effects of geometry on molecule mobility observed in Figure 3-6. Figures 3-7 and 3-8 show that more time is spent in the deep region (and in particular, trying to enter the shallow region) of the *idealized* geometry compared to the more *realistic* geometry, suggesting that the effect of the geometry on the effective energy barrier contributes to the mobility difference significantly. Note that these plots were generated with the same q'_{ref} (namely $q'_{ref} = 4.3 \times 10^{-11}\frac{C}{m}$) to ensure that the increased q'_{ref} in the idealized geometry is not the reason for the observed discrepancy.

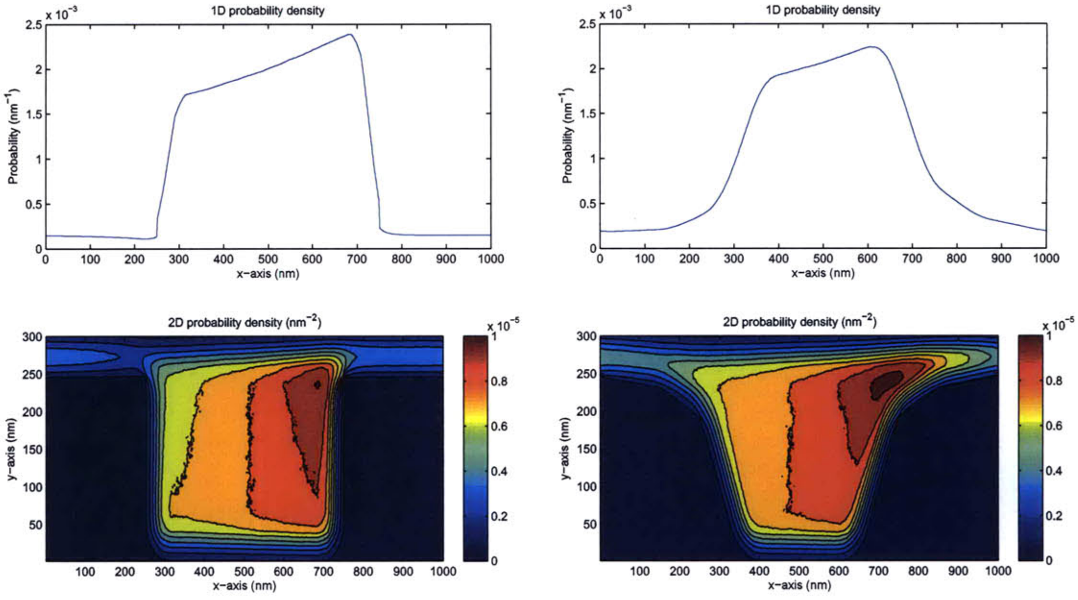

(a) Idealized geometry.

(b) Realistic geometry.

Figure 3-7: Probability density distribution for $L = 108\ nm$, $E_{av} = 63.4\ V/cm$.

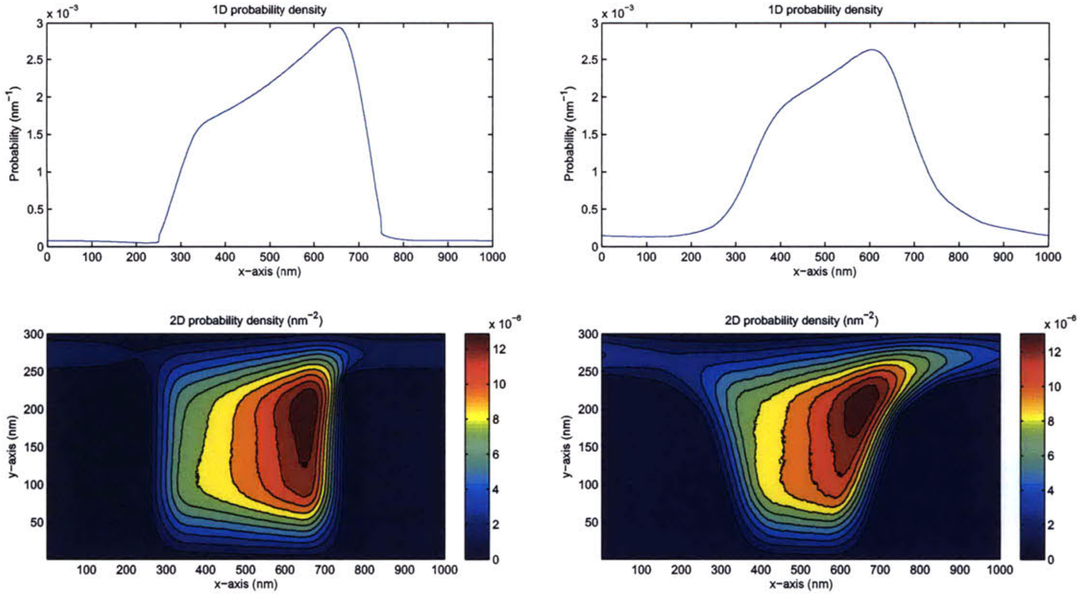

(a) Idealized geometry.

(b) Realistic geometry.

Figure 3-8: Probability density distribution for $L = 216\ nm$, $E_{av} = 63.4\ V/cm$.

3.9 Separation using asymmetric devices

In this section we discuss simulations of electrophoretic motion in asymmetric devices. This study is motivated by recent theoretical results [67] suggesting that comparable separation using a significantly shorter device can be achieved using asymmetric devices (see Figure 3-9) in conjunction with an electric field of alternating polarity. This proposal is based on the observation that the asymmetry in the device geometry will result in different mobilities in the two directions of travel which can be explored using an alternating electric field, to yield a macroscopic drift. In particular, the device shown in Figure 3-9 uses the observation that a slanted wall reduces the entropic barrier for travel in one direction significantly while leaving the entropic barrier for travel in the other direction essentially unchanged.

The model of Li et al. [67] treats DNA molecules as rigid rods and models them as point particles by accounting for their orientational configurations and resulting steric hindrance using a local partition coefficient. Assuming absence of torques due to electrostatic effects, and dominant diffusion, a one-dimensional advection-diffusion equation is formulated and numerically solved. The assumption of dominant diffusion also requires [67] that the characteristic time associated with the voltage oscillation period is long compared to the time taken for traversing one geometrical period. To validate the main theoretical prediction of Li et al. but also investigate how a more realistic representation (e.g. finite chain stiffness, three-dimensional geometry, significantly longer molecules) modifies their results, we performed Brownian Dynamics simulations using the model described above. We focus on the case $\theta = \pi/4$ with $d_s = 60\ nm$, $d_d = 240\ nm$, $L_s = L_d = 500\ nm$. Results for the net molecule velocity for three electric field strengths ($100\ V/cm$, $200\ V/cm$, $400\ V/cm$) are shown in Figure 3-10. For the results shown here, the electric field is of the form of a square wave of frequency $f = 0.1\ Hz$. Other simulations, not shown here, have established that, as expected, the net molecule velocity is independent of the oscillation frequency, provided that $1/f$ is long compared to the time taken by the molecule to traverse one geometric period (p). The results support the main conclusion of Li et al., namely that asymmetry can be exploited to achieve separation. Our model also shows that the molecule mobility appears to increase monotonically with molecule length well beyond the rigid-rod regime. Saturation is visible for long molecules/high electric fields; in fact, it appears that the controlling variable is the product of E and L, or in other words Pe_t. Our results suggest that saturation occurs for $Pe_t \gtrsim 27.3$. Figure 3-11

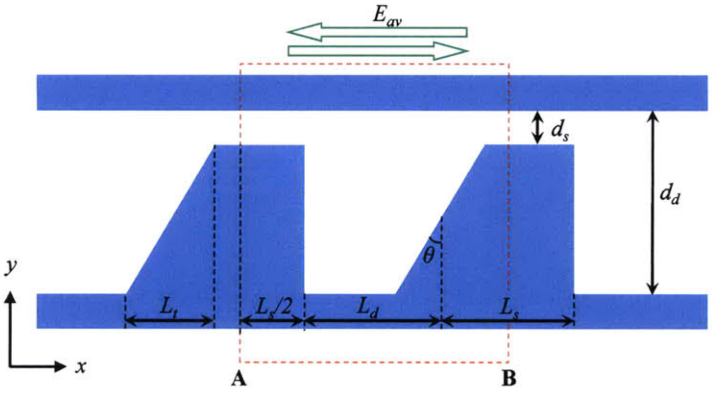

Figure 3-9: Schematic of one period of the asymmetric nanofilter array.

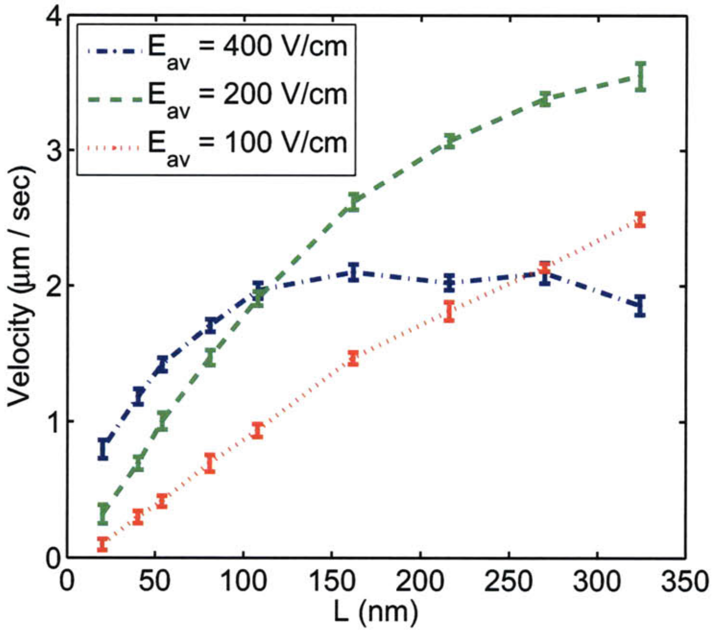

Figure 3-10: Net velocity of dsDNA molecules of different lengths in asymmetric device under AC fields of varied strength.

shows the probability density of the DNA molecule ($L = 270\ nm$, $E_{av} = 100\ V/cm$, $Pe_t = 17.8$) as it is traveling through the asymmetric channel under the action of an AC field. As expected, the figure shows that molecules spend a longer time trying to enter the narrow region when traveling to the left than when traveling to the right.

3.10 Discussion

We have presented an efficient BD model of electrophoretic short-dsDNA-molecule separation in nanofluidic devices. Our results show that both the separation efficiency and molecule mobility are sensitive to the device geometry, with the latter exhibiting a difference on the order of 40% between the idealized and a more realistic geometry. The model achieves good agreement with the experimental results of Fu et al. using only one adjustable parameter. A more accurate comparison with experimental data requires a more precise characterization of the *actual* system geometry as well as the associated variability between different periods, as well as more accurate character-

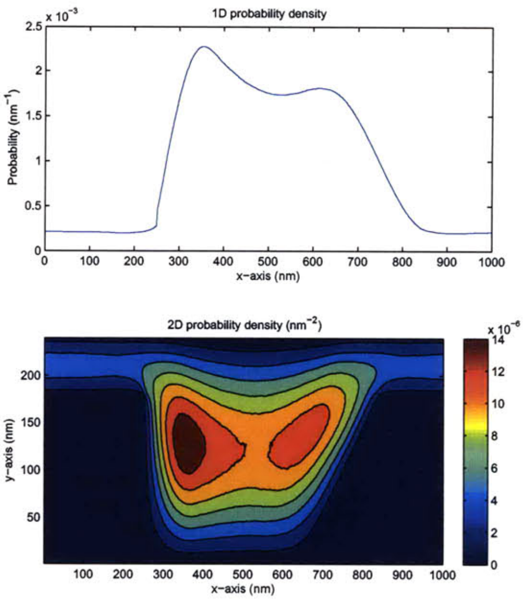

Figure 3-11: Probability density distribution in asymmetric channel with AC field for $L = 270\ nm$, $E_{av} = 100\ V/cm$ ($Pe_t = 17.8$).

ization of other system parameters (e.g. electric field strength, electroosmotic flow magnitude).

The mobility differences between the two geometries studied here are in line with the conclusions of previous theoretical treatment of rigid rod molecules [67] which shows that wall tapering increases molecule mobility, both in an absolute sense but also as a function of molecule length, with longer molecules experiencing a larger increase in mobility. For the conditions studied in [67] (short molecules and low to medium electric field) this behavior was primarily attributed to the reduction of the effective energy barrier as a result of the tapered geometry.

Simulations in asymmetric devices in the presence of an electric field of alternating polarity show a monotonic increase of molecule mobility with molecule length, essentially verifying the prediction by Li et al. [67] for short molecules. Saturation and thus loss of selectivity is observed for $Pe_t \gtrsim 27.3$.

The model presented here is sufficiently accurate to be useful for the design of new separation devices as well as evaluation and optimization of newly proposed devices, such as the two-dimensional device shown in Figure 1-3 which achieves continuous separation [3].

Chapter 4

Rigid-rod model

4.1 Introduction

In the previous Chapter we showed that a Worm-Like-Chain model can achieve reasonable agreement with experimental data. In this section we show how one can take advantage of the fact that molecules with lengths on the order of, or smaller than, one persistence length can be treated as rigid to develop an even more efficient simulation tool based on the rigid-rod model. Moreover, by comparing our results with those of WLC model (Chapter 3) we obtain useful information on the validity of the rigid-rod approximation.

4.2 The rigid-rod model

In the rigid-rod model, the DNA molecules are modeled as non-interacting rigid rods (length L, hydrodynamic diameter $D_h = 2.6\ nm$ [68]) moving under the action of electric field in the geometry of Figure 1-5 with the typical dimensions given. The rod conformation at time t is specified by the position vector $\mathbf{r}$ of its center of mass and the unit vector $\hat{\mathbf{u}}$ along the axis of the rod (see Figure 4-1). The rod translational velocity $\mathbf{v}$ and angular velocity $\boldsymbol{\Omega}$ are defined by

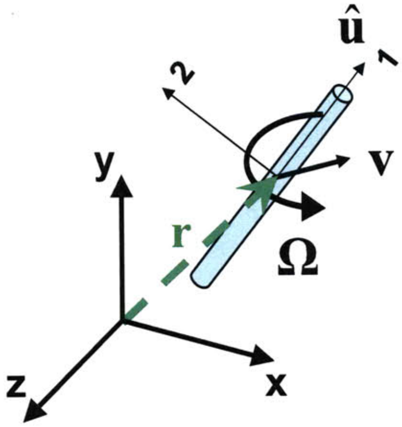

Figure 4-1: Rigid rod-like model.

$$\mathbf{v} = \frac{d\mathbf{r}}{dt} \tag{4.1}$$

$$\boldsymbol{\Omega} = \hat{\mathbf{u}} \times \frac{d\hat{\mathbf{u}}}{dt} \tag{4.2}$$

The Langevin equations of motion for translation and rotation of *thin* rods can be written as

$$\dot{\mathbf{p}} = -\boldsymbol{\Xi} \cdot \dot{\mathbf{r}} + \mathbf{F}^{(systematic)} + \mathbf{F}^{(random)} \tag{4.3}$$

$$\dot{\mathbf{J}} = -\boldsymbol{\Lambda} \cdot \boldsymbol{\Omega} + \mathbf{T}^{(systematic)} + \mathbf{T}^{(random)} \tag{4.4}$$

where $\mathbf{p}$ and $\mathbf{J}$ are the linear and angular momentum of the rod, respectively. The drag force exerted by the surrounding fluid is accounted for by $-\boldsymbol{\Xi} \cdot \dot{\mathbf{r}}$ for the translational part and by $-\boldsymbol{\Lambda} \cdot \boldsymbol{\Omega}$ for the rotational part. $\mathbf{F}^{(systematic)}$ is a systematic force due to the external electric field and $\mathbf{T}^{(systematic)}$ is a systematic torque again due to the external electric field. Finally, the effects of the randomly fluctuating forces exerted on the rod by the surrounding fluid are modeled by a random force $\mathbf{F}^{(random)}$ and a random torque $\mathbf{T}^{(random)}$.

Both the translational ($\boldsymbol{\Xi}$) and rotational ($\boldsymbol{\Lambda}$) drag tensor are orientation dependent and can be written as:

$$\mathbf{\Xi} = \zeta_{\|}\hat{\mathbf{u}}\hat{\mathbf{u}} + \zeta_{\perp}(\hat{\mathbf{I}} - \hat{\mathbf{u}}\hat{\mathbf{u}}) \tag{4.5}$$

$$\mathbf{\Lambda} = \zeta_r(\hat{\mathbf{I}} - \hat{\mathbf{u}}\hat{\mathbf{u}}) \tag{4.6}$$

where $\zeta_{\|}$ and $\zeta_{\perp}$ are the friction coefficients for motions parallel and normal to the rod axis and ζ_r denotes the friction coefficient for rotational motion (about a principal axis with non-negligible moment of inertia). The standard drag models for a slender rod can be summarized as follows [40]

$$\zeta_{\|} = \frac{2\pi\eta_s L}{\ln(L/D_h) + \gamma_{\|}(L)} \tag{4.7}$$

$$\zeta_{\perp} = \frac{4\pi\eta_s L}{\ln(L/D_h) + \gamma_{\perp}(L)} \tag{4.8}$$

$$\zeta_r = \frac{\pi\eta_s L^3}{3[\ln(L/D_h) + \gamma_r(L)]} \tag{4.9}$$

where η_s is the solvent viscosity and $\gamma_r(L) = -0.662 + 0.917(D_h/L) - 0.050(D_h/L)^2$ introduces a correction for the rotational friction coefficient in order to fit the experimental data of sedimenting short DNA fragments as predicted by Tirado et al. [68]. Here, in the interest of simplicity, we assumed that the parallel and normal direction to the rod have the same correction factor ($\gamma_t(L) = \gamma_{\|}(L) = \gamma_{\perp}(L)$); this leads to a simple analytical expression for the average friction coefficient ζ_{av} [53]

$$\zeta_{av} = 3\left(\frac{1}{\zeta_{\|}} + \frac{2}{\zeta_{\perp}}\right)^{-1} = \frac{3}{2}\zeta_{\|} \tag{4.10}$$

We found $\gamma_t(L) = -1.913 + 12.196(D_h/L) - 27.739(D_h/L)^2$ provides the best correction for the translational friction coefficient for finite rod length such that the rod model average diffusion coefficient matches the experimental data fit for the diffusion coefficient of short dsDNA molecules of Lukacs et al. [7].

4.3 Systematic forces and torques

The electrostatic forces and torque on the DNA molecule are calculated by computing forces on the molecule due to its effective charge. The effective charge is assumed to be uniformly distributed between six equidistant sites along the molecule length. (We have verified that our results do not change appreciably by increasing the number of sites.) The electric field in the channel is calculated "offline" using the MATLAB *Partial Differential Equation Toolbox* as it was discussed in Section 3.3.1.3.

Despite the fact that the electrostatic torque is included in our model, in the regime studied here it has a small effect. The effect of this torque and its contribution to molecule escape is extensively discussed by Laachi et al. [19]. The rotational Péclet number comparing the effect of this torque to thermal fluctuations is defined and given in Equation 2.10. In our case, rotational Péclet number is much smaller than 1, which implies that torque effects are small [19]. This is verified by our simulations (see Section 4.7.1)

4.4 Integration scheme

Standard BD techniques [38, 26, 40, 39] are used for integrating the equations of motion. The translational equation of motion is integrated for a time step Δt using

$$\mathbf{r}(t+\Delta t) = \mathbf{r}(t) + \Xi^{-1}(t)\cdot \mathbf{F}(t)^{(systematic)}\Delta t + \mathbf{R}_r \tag{4.11}$$

where $\Xi^{-1}(t)$ and $\mathbf{F}(t)^{(systematic)}$ are calculated for the given conformation at t as described in previous Sections 4.2 and 4.3. The random displacements $\mathbf{R}_r$ are chosen from a Gaussian distribution with the moments

$$\langle \mathbf{R}_r \rangle = 0 \tag{4.12}$$

$$\langle \mathbf{R}_r \otimes \mathbf{R}_r \rangle = 2k_BT\Xi^{-1}(t)\Delta t \tag{4.13}$$

Similarly, the rotational equations of motions are integrated as follows:

$$\hat{\mathbf{u}}(t + \Delta t) = \hat{\mathbf{u}}(t) + \mathbf{\Lambda}^{-1}(t) \cdot \left[\mathbf{T}(t)^{(systematic)} \times \hat{\mathbf{u}}(t)\right] \Delta t + \hat{\mathbf{U}}_r \tag{4.14}$$

where $\mathbf{\Lambda}^{-1}(t)$ and $\mathbf{T}(t)^{(systematic)}$ are calculated for a given conformation at time t as described in the previous Sections 4.2 and 4.3. The random rotations $\hat{\mathbf{U}}_r$ is the sum of two orthogonal gaussian reorientations and perpendicular to $\hat{\mathbf{u}}(t)$. We normalize the new orientation vector $\hat{\mathbf{u}}(t)$, since the integration step will slightly modify its length. The normally distributed random rotations $\hat{\mathbf{U}}_r$ have the following moments:

$$\left\langle \hat{\mathbf{U}}_r \right\rangle = 0 \tag{4.15}$$

$$\left\langle \hat{\mathbf{U}}_r \otimes \hat{\mathbf{U}}_r \right\rangle = 2k_B T \mathbf{\Lambda}^{-1}(t) \left(\hat{\mathbf{I}} - \hat{\mathbf{u}}\hat{\mathbf{u}}\right) \Delta t \tag{4.16}$$

4.5 Boundary condition

Interactions with the walls are steric; in other words, if during a move, part of the molecule extends beyond one of the system boundaries, the move is rejected. In such a case, the molecule is assigned its original position, and forces are recalculated to give a new position which is again checked for boundary crossing. This is the same treatment we used for the Worm-Like-Chain model and similar to the work of several researchers [23, 19]. Again, we have considered both including and neglecting the time increment during rejected moves; the difference to our results is negligible due to the small timestep used which results in a number of rejected steps that is less than 1% of the total number of steps.

4.6 Simulation parameters

Similar to the Worm-Like-Chain model, to calculate the force due to the electric field we use the concept of DNA effective charge. This concept is necessary because due to a variety of complex electrostatic interactions between the DNA and the surrounding solvent [69, 70], a significant part of the DNA's charge is screened, leading to a mobility that is significantly smaller than the expected value based on the molecule charge.

One convenient way of capturing the essence of these effects without using *ab initio* models which would render the simulation intractable, is to define an effective charge that can be calculated from the observed experimental behavior. Similarly to the Worm-Like-Chain model, and as discussed in detail in Section 3.7.1, the molecule effective charge per unit length varies with L such that the observed (free-draining) experimental mobility is independent of the molecule length. In other words we let

$$q'_{rod}(L) = \frac{[\ln(L_p/D) + \gamma_t(L_p)]}{[\ln(L/D) + \gamma_t(L)]} q'_{ref} \tag{4.17}$$

where q'_{ref} is the effective charge of the DNA molecule of one persistence length ($L_p = 54\ nm$), as defined in section 3.7.1.

4.7 Simulation results

Figure 4-2 shows a comparison between the rigid-rod and WLC model results for the ideal geometry. The physical parameters were chosen such that the two models have equivalent charge per unit length and drag. As, expected, the rigid-rod and WLC models are in very good agreement for $L \lesssim 54\ nm$ ($\simeq L_p$). The error for $L \approx 108\ nm(\simeq 2L_p)$ is on the order of 10% and increases as L increases. Similarly, Figure 4-3 shows a comparison between the rigid-rod and WLC results for the more realistic geometry. Again, the rigid-rod and WLC models are in very good agreement for $L \lesssim 54\ nm$ ($\simeq L_p$). The error for $L \approx 108\ nm(\simeq 2L_p)$ is on the order of 10% and increases as L increases. Hence the range of applicability of this model depends on the amount of modeling error that can be tolerated but in general, we can state that this model, as expected, is applicable for molecules with length on the order of, or smaller than, the persistence length. This is in agreement with the observation of Fu et al. [4]

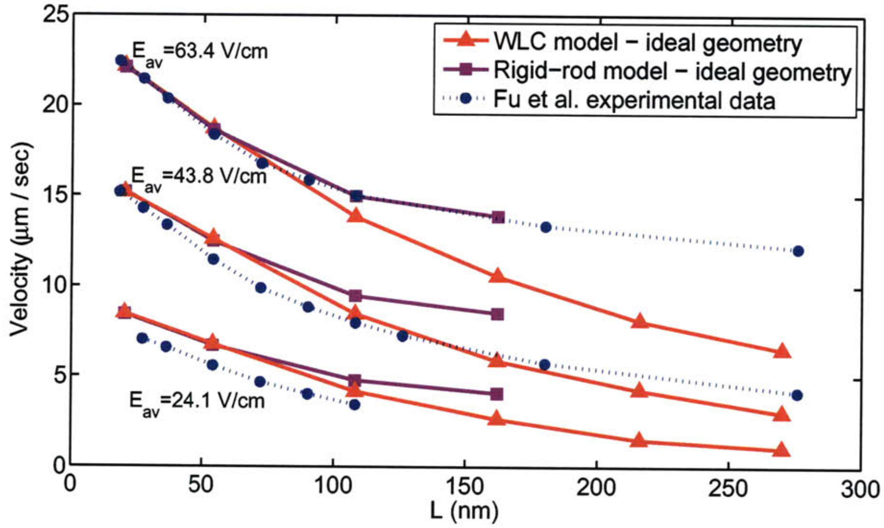

Figure 4-2: Comparison between WLC and rigid-rod model results (ideal geometry).

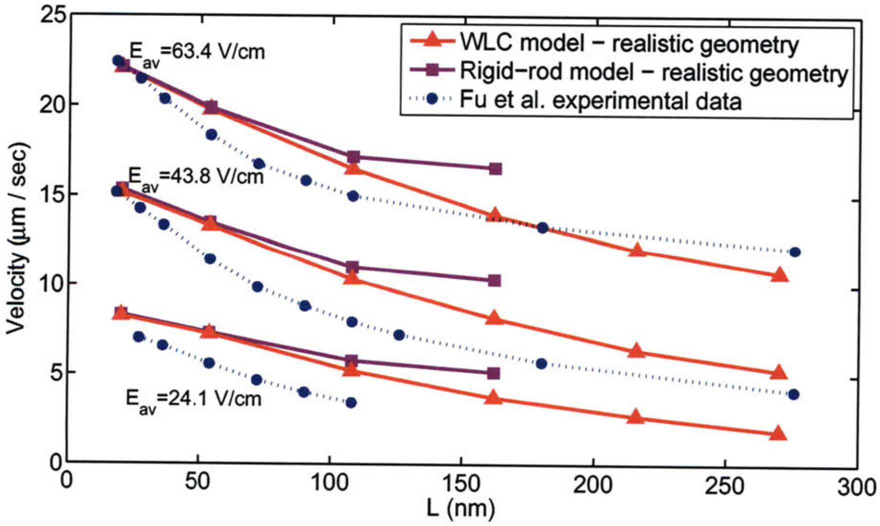

Figure 4-3: Comparison between WLC and rigid-rod model results (realistic geometry).

and consistent with previous work [71] based on a continuum transport model which utilizes the statistical theory of Giddings to characterize the entropic barrier; the latter work also finds that for $L < 100\ nm$ agreement with the experimental results of Fu et al. is good but for $L \approx 100\ nm$ some discrepancy is visible. It should thus be preferable for molecules satisfying this condition since it is faster than the WLC model since it only requires four versus $3\,N$ degrees of freedom (N is the number of beads) for the Worm-Like-Chain model. For example, for a 54 nm DNA molecule the rigid-rod model is four times faster than the WLC model. Moreover, the resulting boundary condition is more simple and easier to implement.

4.7.1 Electrostatic torque effects

Since the rotational Péclet number is much smaller than unity, and as discussed in Section 4.3, the torque effects are expected to be small and will not affect the DNA mobility. Figure 4-4 verifies this by comparing results between simulations which include and simulations which do not include electrostatic torque effects. These simulations were performed in the ideal geometry; similar results are obtained in the realistic geometry.

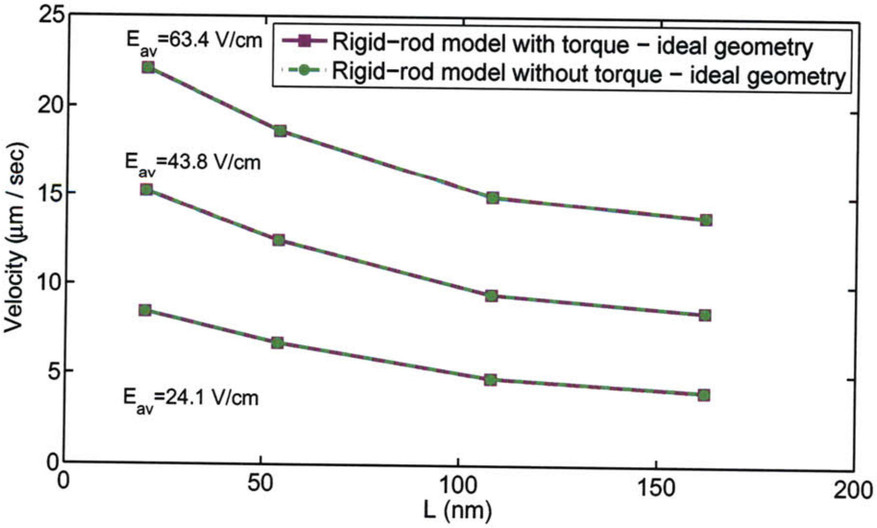

Figure 4-4: Torque effect on DNA mobility (ideal geometry).

4.8 Summary, advantages and limitations

We have presented a rigid-rod model for short DNA molecules. The model is simpler and more efficient than the Worm-Like-Chain model of Chapter 3. The improved efficiency is a result of a number of factors including:

1. significantly simplified equations of motion and much simpler integration algorithm,
2. reduction in degrees of freedom (four versus $3N$ beads for the Worm-Like-Chain model),
3. a simplified boundary condition that is more efficient to implement.

These factors result in an implementation that is at least 4 times more efficient than the corresponding Worm-Like-Chain, which produces essentially indistinguishable results for short DNA molecules (i.e. $L \lesssim 54\ nm\ (\simeq L_p)$).

Chapter 5

Simple partition-coefficient-based model

In this Chapter we continue to exploit various features of short molecules to develop even more efficient simulation methods than the one presented in Chapter 4. Specifically, we develop a new Brownian Dynamics model for predicting the mobility of short molecules, by treating them as Brownian *point particles* and incorporating the effect of their rotational degrees of freedom into an entropy penalty term which modifies the free energy landscape to which the particles are subject to. Such an approach is possible because for the short molecules considered here, the rotational Péclet number is very small ($Pe_r < 0.05 \ll 1$ – see section 2.1.2) suggesting that equilibration of the rotational degrees of freedom is very fast. In other words, the number of rotational states available to molecules can be approximated by equilibrium partition coefficients [41] which are easy to calculate either analytically [72] or off-line.

As we show below, the resulting Brownian Dynamics formulation is significantly more efficient than the equivalent rigid-rod simulation model with no perceptible deterioration in fidelity, as quantified by comparison with the experimental data of Fu et al. [4].

5.1 Energy Landscape

The partition-coefficient approach has been recently used within a Fokker-Planck framework [41] to predict molecular mobilities in periodic devices. As stated above, it uses equilibrium partition coefficients to calculate an entropic barrier that modifies the energy landscape experienced by the molecule as it moves in the device. This landscape is shown in Figure 5-1. The free energy can be decomposed into two parts [4, 41]:

1. electrostatic contribution due to the electric potential drop across channel, and
2. entropic contribution that we will discuss in detail below.

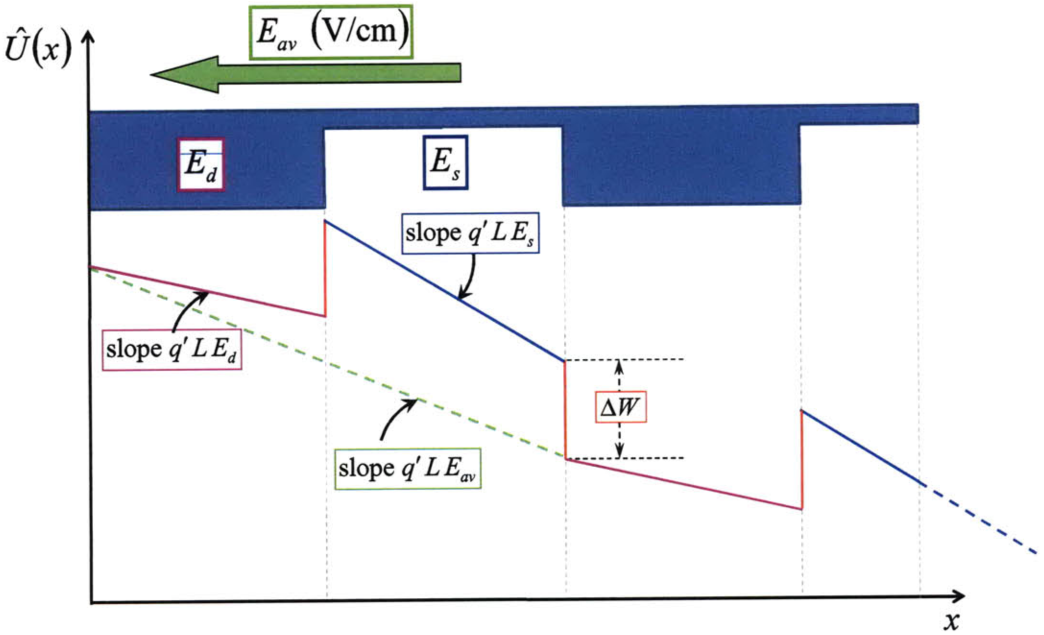

Figure 5-1: Energy landscape of a charged DNA molecule along the nanofilter channel.

5.1.1 Electrostatic Energy

In this model the two-dimensional electric field is approximated by two piecewise constant one-dimensional effective fields, E_d and E_s in the deep and shallow regions, respectively. We note that this approximation is not necessary nor related to the main modeling approximation introduced in the next subsection. It is included here for the purpose of evaluating its effect.

Applying a resistance in series model we obtain the following expressions for the electric field in the deep and shallow regions

$$E_d = \frac{\epsilon(1+\nu)}{\epsilon+\nu} E_{av} \tag{5.1}$$

$$E_s = \frac{1+\nu}{\epsilon+\nu} E_{av} \tag{5.2}$$

where $\epsilon = d_s/d_d$ is the depth ratio (shallow to deep region) and $\nu = l_s/l_d$ is the length ratio between the shallow and deep region [41]. Based on this, for the first period, the electrostatic free energy varies as follows:

$$\hat{U}_E(x) = \begin{cases} q'(L)LE_d x & 0 < x < l_d \\ q'(L)LE_d l_d + q'(L)LE_s(x - l_d) & l_d < x < l_d + l_s \end{cases} \tag{5.3}$$

5.1.2 Entropic Barrier

As in previous Chapters, molecule interactions with the walls are steric; in other words, if part of the molecule extends beyond one of the system boundaries, the configuration is not allowed. Based on our steric boundary conditions, a rigid-rod like DNA molecule near a wall is not entirely free to rotate since certain angular configurations are forbidden, because they entail a partial overlap with the wall. We account for these partial exclusions using $\kappa(\mathbf{r})$ [72], which is defined as the local orientation partition function. This function measures the ratio of the number of occurrences of mass centers at position $\mathbf{r}$ relative to the free solution. Following references [72], [41], we define K_d and K_s to be the average partition coefficient for the deep and shallow region, respectively. K_d and K_s measure the probability of finding a molecule in the deep and shallow regions of the channel, respectively, relative to that in bulk solution. Mathematically, we can write

$$K_d = \frac{\iiint_{V_d} \kappa(\mathbf{r}) d^3\mathbf{r}}{\iiint_{V_d} d^3\mathbf{r}} \tag{5.4}$$

$$K_s = \frac{\iiint_{V_s} \kappa(\mathbf{r}) d^3\mathbf{r}}{\iiint_{V_s} d^3\mathbf{r}} \tag{5.5}$$

where V_d and V_s denote the volume of the deep and shallow regions of the nanofilter, respectively. These quantities can be evaluated either analytically when possible (e.g. [72]) or by direct enumeration (simulation) [41]. Let us also define $K = K_s/K_d$, which describes the ratio of probabilities of occurrence of the DNA molecule in the shallow region compared to the deep region (at *equilibrium*). Following these definitions, the change of free energy from deep to shallow region due to orientational effects is given by [72, 4, 41]:

$$\Delta W = -T\Delta S \tag{5.6}$$

where the entropy term is given by $\Delta S = k_B \ln(K_s/K_d) = k_B \ln(K)$; hence the entropic contribution to the energy barrier is:

$$\Delta W = -k_B T \ln(K) \tag{5.7}$$

5.2 Brownian Dynamics implementation

Li et al. [41] used this formulation within a Fokker-Planck setting [38, 73] describing the time evolution of the probability density function $P(\mathbf{r}, t)$ for the Brownian particle appearing at point $\mathbf{r}$ in the device at time t. Reducing this description to a quasi-one dimensional geometry and using macrotransport theory [74], Li et al. [41] derived an explicit analytical solution for the effective Ogston mobility in the nanofilter array. In a later publication, [75] Li et al. provided a finite difference numerical solution of the Fokker-Planck description in the two dimensional channel geometry, aiming to quantify the error associated with the projection from 2D to 1D. Comparing their 1D analytical to their more accurate 2D solution, Li et al. found that their 1D model overestimates the molecule mobility by $10 - 20\%$.

Our present formulation builds on the work of Li et al. [41] by incorporating the entropic barrier formulation of equations 5.4 - 5.6 into a Brownian Dynamics simulation. This avoids the difficulties associated in the one-dimensional projection and the associated modeling error, while resulting in a formulation that is simple and more efficient than the numerical solution of the Fokker-Planck system in two spatial dimensions.

The motion of a Brownian particle is described by the Langevin equation

$$\dot{\mathbf{p}} = -\boldsymbol{\Xi} \cdot \dot{\mathbf{r}} + \mathbf{F}(t)^{(systematic)} + \mathbf{F}(t)^{(random)} \tag{5.8}$$

where $\mathbf{p}$ is the linear momentum. The drag force exerted by the surrounding fluid is accounted for by $-\boldsymbol{\Xi} \cdot \dot{\mathbf{r}}$. $\mathbf{F}(t)^{(systematic)} = -\nabla \hat{U}_E(x)$ is the systematic force due to the external electric field. The effects of the randomly fluctuating forces exerted on the molecules by the surrounding fluid are modeled by a random force $\mathbf{F}^{(random)}$ which is drawn from a Gaussian distribution with the following moments:

$$\left\langle \mathbf{F}(t)^{(random)} \right\rangle = 0 \tag{5.9}$$

$$\left\langle \mathbf{F}(t)^{(random)} \mathbf{F}(t_0)^{(random)} \right\rangle = 2k_B T \boldsymbol{\Xi} \delta(t - t_0) \tag{5.10}$$

Here $\delta(t - t_0)$ is the Dirac delta function. The translational drag tensor is given by $\boldsymbol{\Xi} = \zeta_{av}\mathbf{I}$, where $\mathbf{I}$ is the identity matrix, and the friction coefficient ζ_{av} is given by 4.10 chosen such that direct comparison with the models of Chapter 3 and 4 can be made.

Finally, we account for the entropic energy barrier that occurs at the transition from deep to shallow region by allowing the Brownian particles to enter from deep to shallow region with a probability $P_{enter} = K$ (equal to the ratio of probabilities of occurrence of the DNA molecule in the shallow region compared to the deep region at equilibrium); this is implemented in the following way: if a Brownian particle tries to go from the deep to the shallow region we draw from a uniform distribution a random number r_{rand} between 0 an 1. If $r_{rand} > K$ the move is rejected (particle is specularly reflected at the boundary between the deep and shallow region); if $r_{rand} \leq K$ the move is accepted (the particle enters narrow region as intended).

5.3 Results and Discussion

Figure 5-2 compares the numerical results of the rigid-rod model (discussed in Chapter 4) and the partition-coefficient-based model for the travel velocity of DNA molecules as a function of their length in the ideal device geometry. Very good agreement is observed between our rigid rod-model and our partition-coefficient-based model. This agreement is quite remarkable given that in addition to the partition coefficient the electric field is also approximated using Equations 5.1 and 5.2 in the partition-coefficient-based simulation.

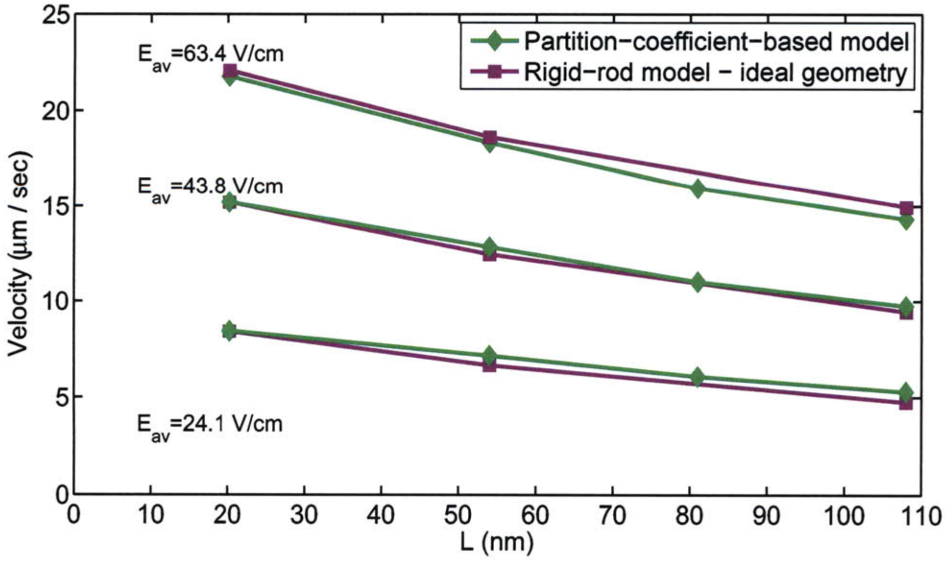

Figure 5-2: Comparison between *the rigid-rod* like model and *the partition-coefficient-based model.*

Figure 5-3 compares the numerical results of the experimental data of Fu et al. [4] and the partition-coefficient-based model for the travel velocity of DNA molecules as a function of their length in the ideal device geometry. We notice good agreement with the experimental data and that the simple-partition coefficient-based model is able to capture *quantitatively* the experimental results despite all the simplification that this model entails.

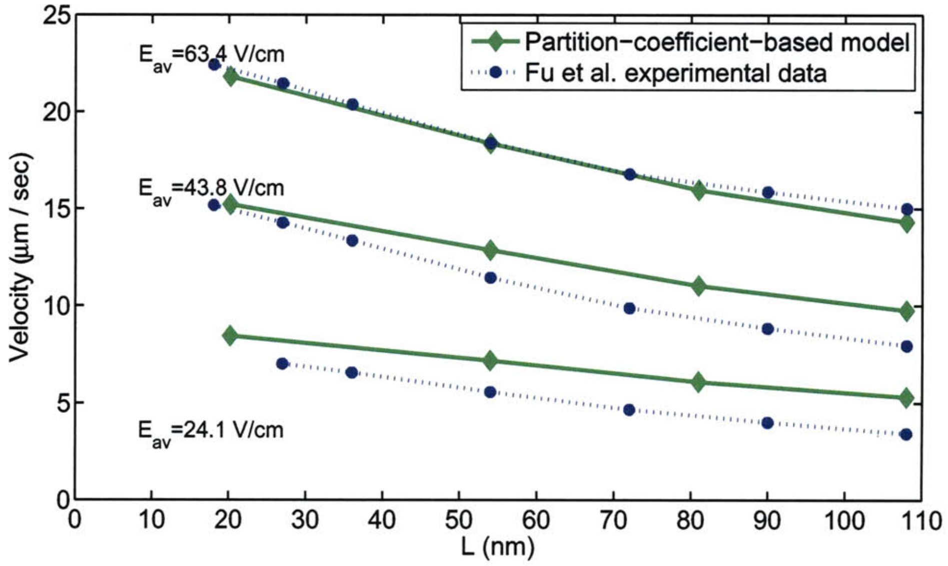

Figure 5-3: Comparison between the experimental data and *the partition-coefficient-based model.*

5.4 Summary, advantages and limitations

We have presented a partition-coefficient-based model for very short DNA molecules. By capturing the effect of rotational degrees of freedom using an entropic penalty term, the resulting model is significantly simpler and more efficient than the rigid rod model of Chapter 4 with no perceptible reduction in fidelity (see Figures 5-2 and 5-3). The improved efficiency is a result of a number of factors including:

1. reduction in degrees of freedom (two versus four for the rigid rod and $3N$ beads for the Worm-Like-Chain model),

2. a significantly simplified boundary condition that is significantly more efficient to implement,
3. a significantly larger time step ($\Delta t = 5e - 7$ s) compared to the rigid-rod model ($\Delta t = 1e - 8$ s). This is possible because the rotational degrees of freedom – the limiting factor in the time step size – have now been eliminated.

These factors result in an implementation that is two orders of magnitude more efficient than the corresponding rigid-rod model, which produces essentially indistinguishable results.

The simplicity of this model makes it ideal for applying variance reduction ideas for reducing the statistical uncertainty associated with its predictions. This is discussed further in the following chapter which shows that significant variance reduction can be achieved for small electric fields. This ameliorates one of the important disadvantages of the Brownian Dynamics approach.

Compared to the Fokker-Planck based work of Li et al., the Brownian Dynamics model presented here is significantly more efficient than the finite difference solution of the Fokker-Planck equation in two dimensions, for the electric fields studied here. Clearly, analytical solutions are always desirable and preferable to simulation results; on the other hand the analytical results of Li et al. [41] suffer from the approximation associated with the projection of the two dimensional Fokker-Planck description to one dimension.

Chapter 6

Variance reduced Brownian Dynamics

6.1 Computational efficiency and variance reduction methods

Although considerably more efficient than alternative approaches (as discussed in Section 2.2), the BD approach of Chapter 5 becomes computationally expensive for low translational Péclet number Pe_t, *especially when very accurate results are required.* This limitation results from the stochastic nature of the model – necessitated by the importance of Brownian effects – which exhibits the standard $1/\sqrt{N_{samples}}$ convergence associated with statistical averaging.

Although the $1/\sqrt{N_{samples}}$ convergence rate is very difficult to alter, especially in the present case where the stochastic fluctuation is imposed by the physics, a number of approaches exist for reducing the number of samples associated with obtaining a certain statistical uncertainty by effectively changing the proportionality constant in the above relation. Such techniques are typically known as variance reduction methods.

The objective of variance reduction techniques is to reduce the statistical uncertainty and thus the computational cost associated with statistical sampling. A number of such methods exist. The one most suited to our formulation is the *control variates* approach originally used by Öttinger et al. [8, 38, 76] where it was referred to as "parallel process simulation". In this approach, the averaged quantity of interest, say the DNA velocity, is evaluated as

$$\bar{V}_{VR} = \bar{V} - \bar{V}_1 + \langle V_1 \rangle \tag{6.1}$$

where $\bar{V}_1$ is the average velocity from an "auxiliary" calculation which (a) uses the same random numbers as the original calculation (the one used to calculate $\bar{V}$), and (b) is such that the expectation value $\langle V_1 \rangle$ is known deterministically.

This technique is successful because the samples used to evaluate $\bar{V}$ and $\bar{V}_1$ are highly correlated (the simulations use the same random numbers) and thus subtracting them leads to significant noise cancelation. A typical choice for the auxiliary calculation is equilibrium (whose moments are typically known analytically). An example of the power of this method is shown in Figure 6-1, adopted from [8], which reports the shear stress in a startup flow of a FENE dumbbell suspension. Figure 6-1 (a) shows that although the signal (for the shear stress in this case) is very noisy (with a standard deviation larger than the available signal), the obvious correlation between the non-equilibrium calculation can be exploited to yield a considerable amount of variance reduction. Comparison with a result obtained by sampling 500 times more dumbbells (Figure 6-1 (b)) suggests that the variance reduction achieved is much larger than a factor of 500.

6.2 Variance reduction using control variates

The above discussion suggests that variance reduction approaches have enormous potential. However, implementing a variance reduction technique for our Brownian

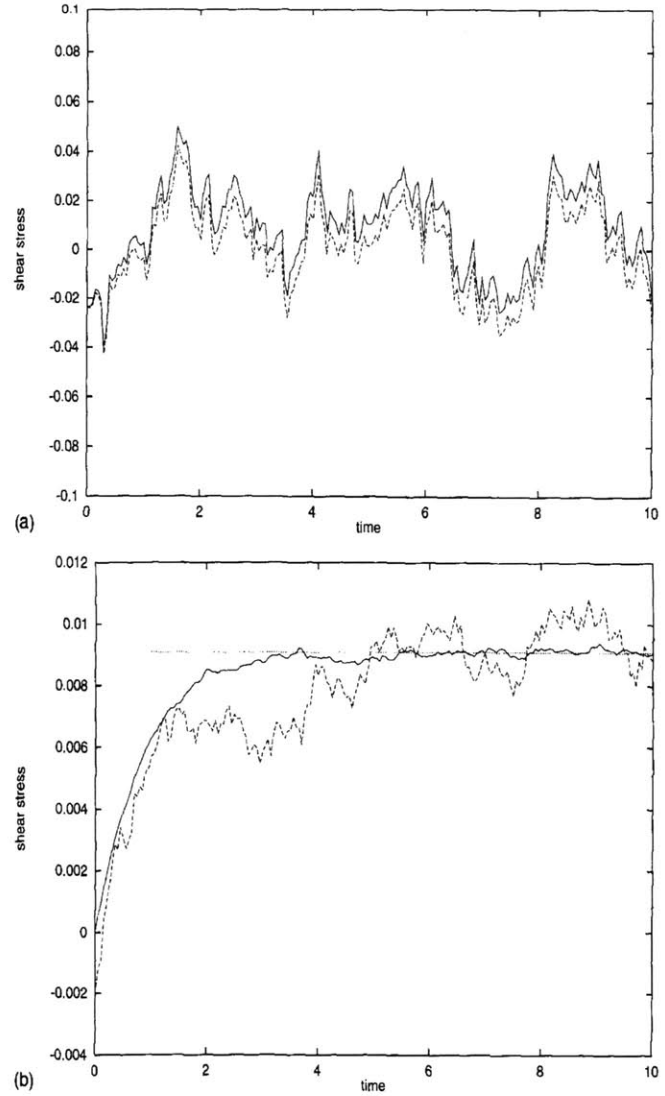

Fig. 1. Start-up of homogeneous shear flow of a FENE dumbbell suspension. (a) The shear stress at $\lambda_H\dot{\gamma} = 0.01$ (solid curve) and in absence of flow (dashed curve). Simulation with 2000 dumbbells with $b = 49$. (b) Shear stress after variance reduction (solid curve) and the results obtained with an ensemble of 10^6 dumbbells (dashed line). The dotted line indicates the exact steady state value.

Figure 6-1: Variance reduction example adapted from Öttinger et al. [8].

Dynamics models is significantly more challenging than the work of Öttinger et al. [8] because of the presence of complex boundary conditions.

Our approach will focus on developing a variance reduction formulation that extends the work of Öttinger et al. [8] to our Brownian Dynamics particle model which includes boundaries. In particular, we will present results from the deviational particle method developed by Baker and Hadjiconstantinou [42, 43] for solving the Boltzmann equation for low-speed gas flow. In addition, we will also extend the work of Al-Mohssen and Hadjiconstantinou ([45, 44]) who used importance weights to formulate variance-reduced methods for solving the Boltzmann equation for low speed gas flow.

In order to describe each method let us consider a simple "canonical" problem, namely Brownian particles moving in one dimension and subject to a constant body force. We are interested in evaluating the average position

$$\langle x \rangle = \int x P(x) dx \tag{6.2}$$

of these particles that are characterized by the non-equilibrium distribution $P(x)$. The standard way to evaluate this integral is by sampling from the non-equilibrium distribution $P(x)$ (importance sampling)

$$\bar{x} = \frac{1}{N} \sum_{i=1}^{N} x_i \tag{6.3}$$

In its most general form, the method of control variates amounts to writing

$$\langle x \rangle = \int x \big[P(x) - P^{aux}(x) + P^{aux}(x) \big] dx \tag{6.4}$$

where $P^{aux}(x)$ is an "auxiliary" distribution chosen carefully in order to satisfy the following requirements:

1. $P^{aux}(x)$ captures most of the variation of $P(x)$ (i.e. $P^{aux}(x) \simeq P(x)$)
2. $\int x P^{aux}(x) dx$ can be evaluated deterministically (analytically or numerically).

The choice of $P^{aux}(x)$ is critical in the sense that the amount of variance reduction achieved depends on how close $P^{aux}(x)$ is to $P(x)$. Fortunately, in the world of molecular simulation methods, this choice is rather simple to make because small signals requiring variance reduction are typically associated with small perturbations from a well defined equilibrium, which is ideally suited for the role of the auxiliary distribution, not only because it is close to the non-equilibrium distribution, but also because its moments are typically easy to calculate if not obvious. In terms of our simple example, we will take $P^{aux}(x) = P^{eq}(x) = const.$ Hence equation 6.4 becomes

$$\langle x \rangle = \int x\big[P(x) - P^{eq}(x) + P^{eq}(x)\big]dx \tag{6.5}$$

We now proceed with two different implementations:

1. Simulate the deviation from equilibrium $\int x[P(x) - P^{eq}(x)]dx$ (see Section 6.2.1). This is the basic idea behind the deviational method first proposed by Baker and Hadjiconstantinou [42, 43] for solving the Boltzmann equation.
2. Use two highly correlated parallel simulations, one simulates $\int xP(x)dx$ and the other $\int xP^{eq}(x)dx$. This method will be referred to as importance-weight method, because it uses importance weights to enable both simulations to use the same random numbers (see Sections 6.2.2).

6.2.1 Variance reduction using deviational particle methods

The deviational particle method can be motivated by writing

$$\langle x \rangle = \underbrace{\int x \underbrace{\big[P(x) - P^{eq}(x)\big]}_{\text{deviational}} dx}_{\text{simulate}} + \underbrace{\int xP^{eq}(x)dx}_{\text{analytical } = \langle x \rangle^{eq}} \tag{6.6}$$

In other words, in this method we use particles to simulate the deviation from equilibrium. The desired estimator of the quantity $\langle x \rangle$ can then be written as

$$\bar{x} = \frac{1}{N}\sum_{i=1}^{N} s_i x_i + \langle x \rangle^{eq} \tag{6.7}$$

where the deviational particle i is located at position x_i and it has the sign s_i (signs are required since $P(x) - P^{eq}(x)$ can be positive or negative). We will discuss the deviational particle method in more detail in Section 6.4.

6.2.2 Variance reduction using importance weights

In the importance-weight method we rearrange 6.5 as follows

$$\langle x\rangle = \underbrace{\int x \underbrace{\frac{P(x)}{P^{eq}(x)}}_{W} P^{eq}(x)dx}_{\text{non-equilibrium}} - \underbrace{\int xP^{eq}(x)dx}_{\text{equilibrium}} + \underbrace{\int xP^{eq}(x)dx}_{\text{analytical } = \langle x\rangle^{eq}} \tag{6.8}$$

This is then interpreted as follows: two parallel simulations are perfomed; the first one is simulating equilibrium $\left(\int xP^{eq}(x)dx\right)$ while the second one evaluates the non-equilibrium quantity $\left(\int x\frac{P(x)}{P^{eq}(x)}P^{eq}(x)dx\right)$ using equilibrium samples through the weights W_i defined as

$$W_i = \frac{P(x_i)}{P^{eq}(x_i)} \tag{6.9}$$

The estimator of the desired quantity can then be written as

$$\begin{aligned} \bar{x}_{VR} &= \bar{x} - \bar{x}^{eq} + \langle x\rangle^{eq} \\ &= \frac{1}{N}\sum_{i=1}^{N} W_i x_i - \frac{1}{N}\sum_{i=1}^{N} x_i + \langle x\rangle^{eq} \\ &= \frac{1}{N}\sum_{i=1}^{N} (W_i - 1)x_i + \langle x\rangle^{eq} \end{aligned} \tag{6.10}$$

Importance weights here is the tool that enables us to effectively simulate two systems (one equilibrium and one non-equilibrium) by simulating only one (in this case the equilibrium); we use the set of weights W_i to provide a "correction" for the number of particles in the non-equilibrium simulation for each particle in the equilibrium simulation. (Clearly for $W_i = 1$, we obtain the equilibrium situation.) We also note that which system (equilibrium/non-equilibrium) is actually simulated and which is inferred through the weights is arbitrary and primarily a matter of convenience. Here we have chosen to simulate the equilibrium and use weights to refer to the non-equilibrium simulation because in equilibrium, reflection of particle positions at no-flux boundaries is higher-order accurate [77]. The inverse choice (i.e. simulating explicitly non-equilibrium) was made in [45], where the objective was to perturb the original simulation as little as possible.

We also note that our task is not complete yet, since the weights W_i are as of now unknown. Successful simulation requires the prescription of evolution rules for updating the weights of particles as those move around the computational domain under the action of the prescribed dynamics and boundary conditions.

6.3 Fokker-Planck description and one dimensional forced diffusion

In the most general case of N interacting Brownian particles, those are described by the Fokker-Planck equation

$$\frac{\partial P}{\partial t} = \sum_{i=1}^{i=N} \sum_{j=1}^{j=N} \frac{\partial}{\partial \mathbf{r}_i} \mathbf{D}_{ij} \left(\frac{\partial P}{\partial \mathbf{r}_j} - \frac{1}{k_B T} \mathbf{F}_j P \right) \tag{6.11}$$

where $P(\mathbf{r}, t)$ is the N-particle configuration space distribution. Here, $\mathbf{D}_{ij}$ represents the configuration dependent diffusion tensor and $\mathbf{F}_j$ is the sum of the inter-particle and external forces on particle j. As stated above, we will look at a simple one-dimensional forced diffusion problem. In this problem, Brownian particles are confined by two non-absorbing walls at $x = 0$ and $x = p$, respectively, and are subject to a uniform field of magnitude U (see Figure 6-2). This system is described by the following

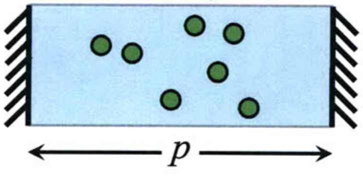

Figure 6-2: One dimensional forced diffusion on non-interacting Brownian particles.

one-dimensional Fokker-Planck equation

$$\frac{\partial P}{\partial t} = -U\frac{\partial P}{\partial x} + D\frac{\partial^2 P}{\partial x^2} \tag{6.12}$$

The no flux boundary condition, at both walls is given by

$$J = -D\frac{\partial P}{\partial x} + UP = 0, \text{ at } \ x = 0, \ p \tag{6.13}$$

For this simple problem we can obtain an analytical solution for the steady state probability distribution $P(x)$ and the average position $\langle x \rangle$. We define Péclet number to be $Pe_t = Up/D$ and we write equation 6.12 in dimensionless form as

$$\frac{\partial P}{\partial \tilde{t}} = -Pe_t\frac{\partial P}{\partial \tilde{x}} + \frac{\partial^2 P}{\partial \tilde{x}^2} \tag{6.14}$$

The no flux boundary condition becomes

$$\tilde{J} = -\frac{1}{Pe_t}\frac{\partial P}{\partial \tilde{x}} + P = 0 \tag{6.15}$$

where $\tilde{x} = x/p$ and $\tilde{t} = tD/p^2$. The steady-state analytical solution for the probability distribution is

$$P(\tilde{x}) = \frac{Pe_t}{\exp(Pe_t) - 1}\exp(Pe_t\,\tilde{x}) \tag{6.16}$$

while the solution of the expectation value of the particle position is

$$\langle \tilde{x} \rangle = \frac{\exp(Pe_t)}{\exp(Pe_t) - 1} - \frac{1}{Pe_t} \tag{6.17}$$

6.4 Simulating 1D forced diffusion using the deviational particle method

In order to simulate the above one-dimensional forced diffusion using the deviational particle method, we note that using $P^{eq}(\tilde{x}) = 1$ and defining $P^d(\tilde{x}) = P(\tilde{x}) - P^{eq}(\tilde{x})$

in 6.14 we obtain

$$\frac{\partial P^d}{\partial \tilde{t}} = -Pe_t \frac{\partial P^d}{\partial \tilde{x}} + \frac{\partial^2 P^d}{\partial \tilde{x}^2} \tag{6.18}$$

or in other words, the Fokker-Planck equation governing deviational particles is the same as the one governing physical particles. From this we conclude that deviational particles behave as physical particles. (Note that this is not generally true, e.g. it is not true if $U = U(x)$ where additional terms appear in Equation 6.18)

6.4.1 Boundary condition

The complexity in this approach arises when considering the boundary condition

$$\tilde{J}^d = -\frac{1}{Pe_t}\frac{\partial P^d}{\partial \tilde{x}} + P^d = -P^{eq} = -1 \tag{6.19}$$

which means that mass conservation requires one negative particle entering the computational domain from the left wall at $x = 0$ ($\tilde{x} = 0$) per unit of dimensionless time per unit of dimensionless area. Similarly we need one negative particle leaving the computational domain per unit time per unit area of the wall at $x = p$ ($\tilde{x} = 1$) as shown in Figure 6-3.

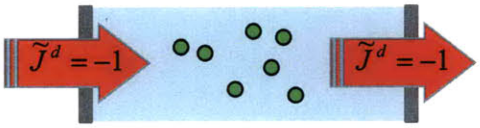

Figure 6-3: No flux boundary condition using deviational particle method.

This boundary condition can be implemented in a variety of ways (e.g. one negative particle entering the domain is equivalent to one positive particle leaving the domain). We illustrate the approach used here with an example: suppose that during one unit of dimensionless time and per one unit of dimensionless area five positive and two negative particles crossed the right wall. In order to satisfy the no flux boundary condition, or in other words to satisfy the dimensionless deviational flux $\tilde{J}^d = -1$, we need to send back four positive particles into the system as shown in Figure 6-4. In other words, our approach consisted of sending one net positive particle into the domain. Thus in the case considered here, the two negative particles cancel the two positive particles leaving us with three positive particles that need to be reflected back to the domain (reflective boundary condition). Adding the net positive particle to those, we have four positive particles entering the computational domain.

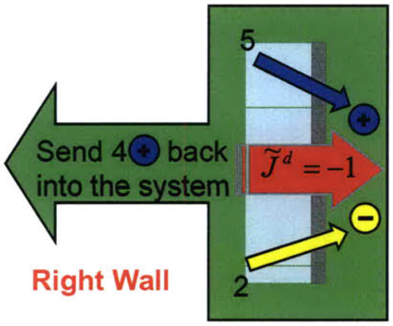

Figure 6-4: Implementation of no flux boundary condition using deviational particles.

6.4.2 Validation

The above implementation was used to obtain a solution for the simple forced diffusion problem 6.12, 6.13. The solution obtained is in excellent agreement with analytical solution 6.17 as shown in Figure 6-5. In the following section we discuss the computational gain achieved by this method.

6.4.3 Computational gain for deviational particle method

As discussed in Section 6.1, regular Brownian dynamics methods exhibit the standard $1/\sqrt{N_{samples}}$ convergence associated with statistical sampling. This means the variance associated with Brownian Dynamics simulations scales as $1/N_{samples}$. The cost of the method is proportional to $N_{samples}$ [1] yielding the relation

$$\text{Var} \propto \frac{1}{N_{samples}} = \frac{1}{\text{computational cost}} \tag{6.20}$$

Given the above, in order to calculate the computational gain in our proposed method it is sufficient to take the ratio of the variances of the two methods. In particular, we

---

[1] assuming the steady state sampling phase dominates the simulation time

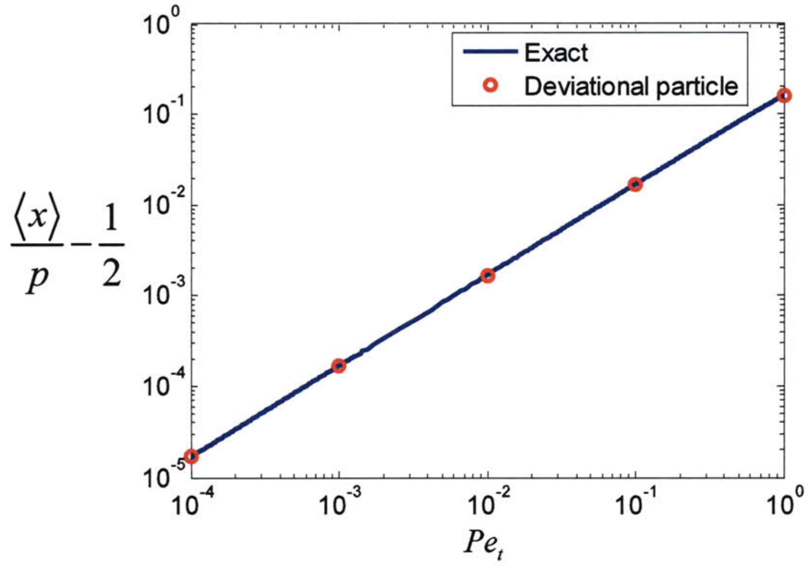

Figure 6-5: Comparing deviational particle results with analytical solution 6.17.

define the computational gain as

$$\text{Computational gain} = \frac{\text{Var}_{RegularBD}}{\text{Var}_{\text{Deviational Particle Method}}} \tag{6.21}$$

This definition clearly assumes that the cost per timestep is similar for the two methods. This is a reasonably valid assumption since both methods presented in this chapter are particularly simple, albeit not as simple as the regular Brownian Dynamics. Figure 6-6 shows the computational gain provided by the deviational particle method. The figure clearly shows that the computational gain provided by the deviational particle method is proportional to Pe_t^{-2} with a proportionality constant such that computational gain is obtained for $Pe_t < 1$.

6.4.4 Limitations of deviational particle method for 2D/3D problems

The proposed deviational particle method provides substantial variance reduction for small translational Péclet number $Pe_t \ll 1$. It is easy to use and implement for one dimensional problems. This technique becomes cumbersome and computationally ex-

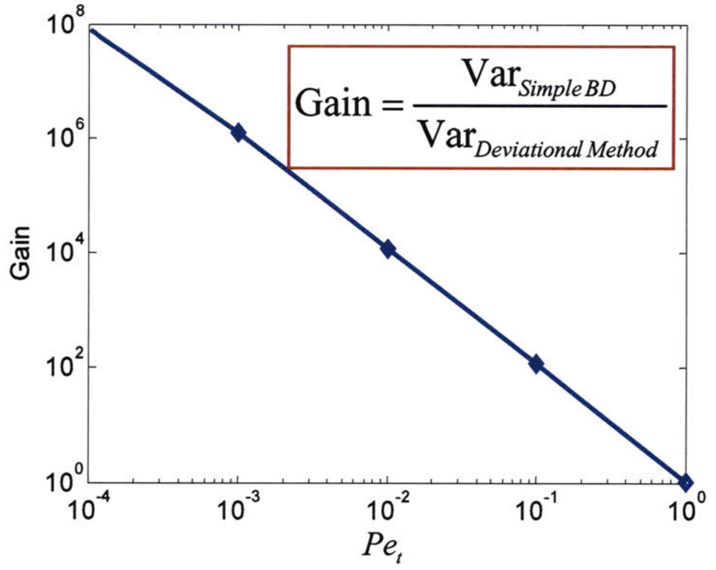

Figure 6-6: Comparing variances of deviational particle method and regular Brownian Dynamics as a function of translational Péclet number.

pensive for 2D and 3D problems because the boundary cancelation process described in Section 6.4.1 needs to be applied *locally* along the boundary, which requires meshing of the latter. Moreover, if $U = U(x)$, deviational particles need to be created volumetrically proportionally to $\frac{dU}{dx}$ which makes the simulation even more cumbersome for arbitrary $U(x)$ (e.g. results from a finite element solution as in Chapter 3).

6.5 Variance reduction using the importance-weight method

Our numerical experiments have shown that an importance-weight formulation is more appropriate for Brownian Dynamics simulations because it leads to a less cumbersome algorithm in higher dimensions. Below we discuss the development of a variance-reduced formulation for the simple one-dimensional forced diffusion problem described in Section 6.3 and the multi-dimensional problem that is the topic of this Thesis.

6.5.1 Weight update rules

In order to simulate 1D forced diffusion using importance weights, we follow the formulation suggested by equations 6.8, 6.9 and 6.10, and simulate an equilibrium simulation (N particles) while at the same time update weights $W_i(t) = 1, \cdots, N$ which keep track of the correlated non-equilibrium simulation.

The equilibrium simulation simulates the motion of N Brownian particles moving in one spatial dimension between two non-absorbing walls at $x = 0$ and $x = p$ as shown in Figure 6-2. Reflecting boundary conditions are imposed, whereby a particle is returned to the domain by taking the mirror image of the "offending" move.

For the non-equilibrium simulation, weights are updated using

$$W_n = W_o \frac{P(x_n, t + \Delta t | x_o, t)}{P^{eq}(x_n, t + \Delta t | x_o, t)} \tag{6.22}$$

where:

W_n: is the new weight of a Brownian particle;

W_o: is the old weight of a Brownian particle;

x_o: is the old position of a Brownian particle;

x_n: is the new position of a Brownian particle;

$P(x_n, t+\Delta t | x_o, t)$: is the non-equilibrium transition probability for a Brownian particle to move to the new position x_n at time $t + \Delta t$ given that the particle old position is x_o at time t;

$P^{eq}(x_n, t + \Delta t | x_o, t)$: is the equilibrium transition probability for a Brownian particle to move to the new position x_n at time $t + \Delta t$ given that the particle old position is x_o at time t.

Equation 6.22 has been first derived in [45] by starting from the definition of the weights, namely

$$W_o = \frac{P(x_o)}{P^{eq}(x_o)} \tag{6.23}$$

and

$$W_n = \frac{P(x_n)}{P^{eq}(x_n)} \tag{6.24}$$

Using the transitional probabilities for one particle we have

$$P^{eq}(x_n, t + \Delta t | x_o, t) = \frac{P^{eq}(x_n)}{P^{eq}(x_o)} \tag{6.25}$$

and

$$P(x_n, t + \Delta t | x_o, t) = \frac{P(x_n)}{P(x_o)} \tag{6.26}$$

Using the above we obtain

$$\begin{aligned} W_n &= \frac{P(x_n)}{P^{eq}(x_n)} \\ &= \frac{P(x_o)\, P(x_n, t + \Delta t | x_o, t)}{P^{eq}(x_o)\, P^{eq}(x_n, t + \Delta t | x_o, t)} \\ &= W_o \frac{P(x_n, t + \Delta t | x_o, t)}{P^{eq}(x_n, t + \Delta t | x_o, t)} \end{aligned} \tag{6.27}$$

which is Equation 6.22.

6.5.2 Initial conditions

Initialization of weights is relatively straight-forward since knowledge of initial conditions of the equilibrium and non-equilibrium calculations is typically part of the problem specification. The initial conditions for the weights follow directly from the definition

$$W_i(t = 0) = \frac{P(x_i, t = 0)}{P^{eq}(x_i, t = 0)}, \text{ for } i = 1, \cdots, N \tag{6.28}$$

In most cases (as in the simple problem considered here) we are interested in the steady state solution, which should be independent of initial conditions. In this case it is most convenient to start from $P(x_i, t = 0) = P^{eq}(x_i, t = 0)$ giving

$$W_i(t = 0) = 1, \text{ for } i = 1, \cdots, N \tag{6.29}$$

6.5.3 Wall bounded simulations

As shown above, dynamic update of weights requires knowledge of the transition probabilities between the old and new states. It is in fact the use of this information that yields a reduced uncertainty (variance reduction). Of course, knowledge of general transition probabilities is equivalent to knowing the solution of the problem of interest, and is thus not useful. Instead, the key to making this approach work is to use transition probabilities that describe the main ingredients of the problem of interest *separately* and synthesize them in a way that the resulting approximation is reasonable. More specifically, the main ingredients of the problems considered here are the external field and the presence of walls. Transition probabilities for Brownian particles in the presence of <u>one wall</u> under the action of a field normal to the wall can be obtained from the famous solution by von Smoluchowski [78, 79].

$$\begin{aligned} P(x_n, t+\Delta t|x_o, t) = &\underbrace{(4\pi\tau)^{-1/2}\exp\big[-(x_n - x_o + b\tau)^2/4\tau\big]}_{\text{pure forced diffusion with no boundary}} \\ &+ \underbrace{(4\pi\tau)^{-1/2}\exp\big[b(x_o - x_w) - (x_n + x_o - 2x_w + b\tau)^2/4\tau\big]}_{\text{boundary effect}} \\ &+ \underbrace{\frac{1}{2}b\ \exp\big[-b(x_n - x_w)\big]\ \text{erfc}\ \big[(x_n + x_o - 2x_w - b\tau)/\sqrt{4\tau}\big]}_{\text{boundary effect}} \end{aligned} \tag{6.30}$$

where x_w is the position of the wall in the direction of the electric field, $b = -U/D$, $\tau = D\Delta t$, and erfc(z) denotes the complementary error function. When $x_o - x_w$, $x_n - x_w \longrightarrow -\infty$ the *boundary effect* part goes to zero and Equation 6.30 simplifies to

$$P(x_n, t+\Delta t|x_o, t) = \underbrace{(4\pi\tau)^{-1/2}\exp\big[-(x_n - x_o + b\tau)^2/4\tau\big]}_{\text{pure forced diffusion with no boundary}} \tag{6.31}$$

We get the transitional probabilities for the equilibrium case from equation 6.30 by setting $b = 0$ (i.e. no external field)

$$P^{eq}(x_n, t + \Delta t | x_o, t) = \underbrace{(4\pi\tau)^{-1/2} \exp\big[-(x_n - x_o)^2/4\tau \big]}_{\text{pure diffusion with no boundary}} + \underbrace{(4\pi\tau)^{-1/2} \exp\big[-(x_n + x_o - 2x_w + b\tau)^2/4\tau \big]}_{\text{boundary effect}} \tag{6.32}$$

Similarly, when $x_o - x_w$, $x_n - x_w \longrightarrow -\infty$ the *boundary effect* part goes to zero and Equation 6.32 simplifies to

$$P^{eq}(x_n, t + \Delta t | x_o, t) = \underbrace{(4\pi\tau)^{-1/2} \exp\big[-(x_n - x_o)^2/4\tau \big]}_{\text{pure diffusion with no boundary}} \tag{6.33}$$

By applying these solutions to a particle between two walls, clearly an approximation is committed. This approximation however, is reasonable if the two walls are sufficiently far apart $\left(p \gg \sqrt{D\Delta t}, |U\Delta t|\right)$, since the particle will only be close to one wall at a time. Knowledge of this solution and judicious use allows us to obtain substantial variance reduction (see. Figure 6-11) while the error from this approximation appears to be small (see Figure 6-8 as well as the next section where this method is applied to the separation process that is the main topic of this Thesis).

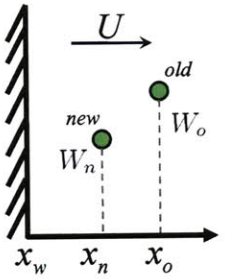

$$W_n = W_o \frac{P(x_n, t + \Delta t | x_o, t)}{P^{eq}(x_n, t + \Delta t | x_o, t)}$$

Figure 6-7: Boundary effects and updating weights.

6.5.4 Validation

Figure 6-8 compares results for the one-dimensional diffusion problem discussed in Section 6.3 to the exact analytical solution given by equation 6.17. Excellent agreement is observed.

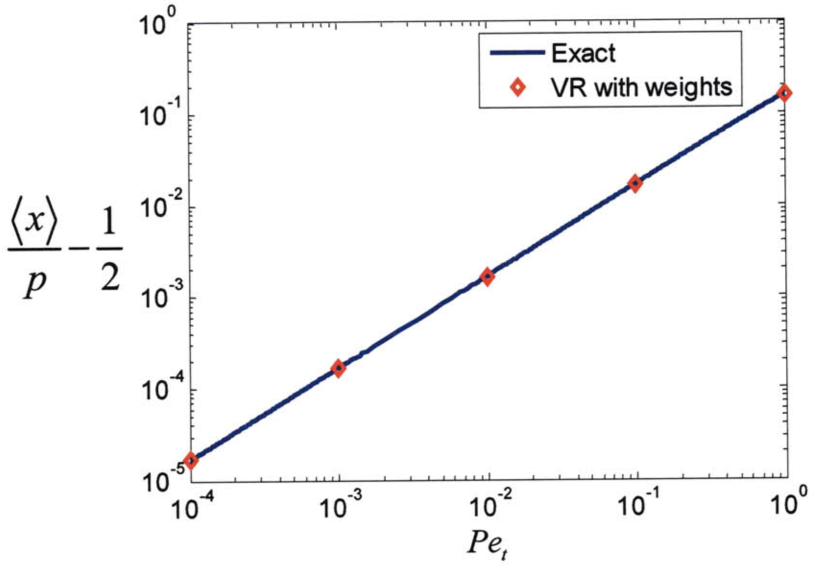

Figure 6-8: Comparing importance-weight method results with analytical solution.

In Section 6.6.2 we discuss the computational gain of the variance-reduced method.

6.6 Application of variance reduction methods to the separation of short biological molecules

The above formulation can be readily extended to the partition-coefficient-based model of Chapter 5. As stated above this is one of the reasons this methodology is preferred. Specifically, to simulate the motion of short DNA molecules using the model of Chapter 5, we run an equilibrium simulation of N non-interacting Brownian particles subject to non-absorbing boundary conditions (reflection). The non-equilibrium calculation is evaluated by using the weight update rules as described in Section 6.5.1. The more complex geometry of this problem (see Figure 6-9) requires us to divide the computational domain into various regions, in order to still use the simple transition probabilities associated with <u>one</u> wall in the direction of electric field.

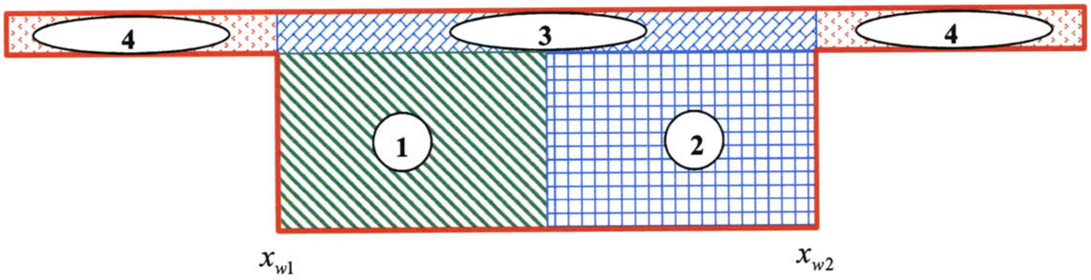

Figure 6-9: Device regions.

We divide the device into four regions, with the following parameters:

- **Region 1**:
  Use Equations 6.30 and 6.32 where $x_w = x_{w1}$, $x_o = x_o$, $x_n = x_n$ and $U = U_d = \frac{E_d q' LD}{k_B T}$
- **Region 2**:
  Use Equations 6.30 and 6.32 where $x_w = -x_{w2}$, $x_o = -x_o$, $x_n = -x_n$ and $U = -U_d$
- **Region 3**:
  Use Equations 6.31 and 6.33 where $x_o = x_o$, $x_n = x_n$ and $U = U_d$
- **Region 4**:
  Use Equations 6.31 and 6.33 where $x_o = x_o$, $x_n = x_n$, $U = U_s = \frac{E_s q' LD}{k_B T}$

where U_d and U_s are the uniform fields due to the electric field in the deep and shallow regions respectively. We always use x_o to determine the region where the particle is located and the parameters to use in the weight update (Equation 6.22).

One special case arises when a molecule steps from the deep to the narrow region. In other words, this special case arises when x_n is in **Region 4** and x_o is in **Region 1**,

2, or **3**. In this special case, as explained in Chapter 5, we account for the entropic energy barrier that occurs at the transition from deep (i.e. the union of **Region 1**, **2** and **3**) to shallow (i.e. **Region 4**) region by allowing the Brownian particles to enter from deep to shallow region with a probability $P_{enter} = K$ (equal to the ratio of probabilities of occurrence of the DNA molecule in the shallow region compared to the deep region at equilibrium); this is implemented in the following way: if a Brownian particle attempts to move from the deep to the shallow region we draw from a uniform distribution a random number r_{rand} between 0 an 1. Then we have the following two cases:

$r_{rand} > K$:

The move is rejected and x_n is now the reflected position (particle is specularly reflected at the boundary between the deep and shallow region). If the particle move was rejected on the right side shallow region entrance, the particle weight is calculated using Equations 6.30 and 6.32 where $x_w = -x_{w2}$, $x_o = -x_o$, $x_n = -x_n$ and $U = -U_d$. Otherwise, if the particle move was rejected on the left side shallow region entrance, the particle weight is calculated using Equations 6.30 and 6.32 where $x_w = x_{w1}$, $x_o = x_o$, $x_n = x_n$ and $U = U_d$.

$r_{rand} \leq K$:

The move is accepted (the particle enters narrow region as intended). The particle weight is calculated using Equations 6.31 and 6.33 where $x_o = x_o$, $x_n = x_n$ and $U = U_d$

6.6.1 Comparison of importance-weight method and regular Brownian Dynamics simulation results

Figure 6-10 compares the simulation results of the importance-weight method to the regular Brownian Dynamics method for the ideal experimental device geometry for a small translational Péclet number. Very good agreement is observed. It is important to note that at the translational Péclet numbers of these simulations ($Pe_t \sim 0.1$), we need over 200 times more samples for the regular method to converge to the same level of statistical uncertainty compared to the importance-weight method. The computational gain provided is discussed in the following section.

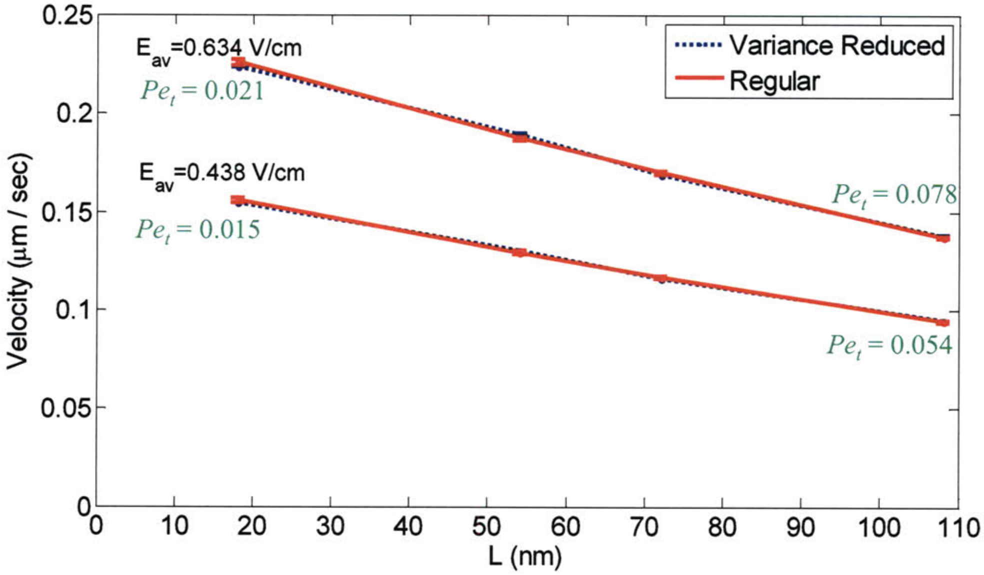

Figure 6-10: Comparing importance-weight results and regular Brownian Dynamics model for small translational Péclet number in the ideal experimental device.

6.6.2 Computational gain for importance-weight method

As discussed in Section 6.4.3, to calculate the computational gain, it is sufficient to take the ratio of the variances between regular Brownian Dynamics method and the importance-weight method, namely

$$\text{Computational gain}_{IW} = \frac{\text{Var}_{RegularBD}}{\text{Var}_{\text{Importance-weight Method}}} \tag{6.34}$$

Figure 6-11 shows the computational gain provided by the importance-weight method. We find that the computational gain is very similar to the deviational particle method and scales as Pe_t^{-2}. As before, the importance-weight method is only superior to the regular Brownian Dynamics method for $Pe_t < 1$.

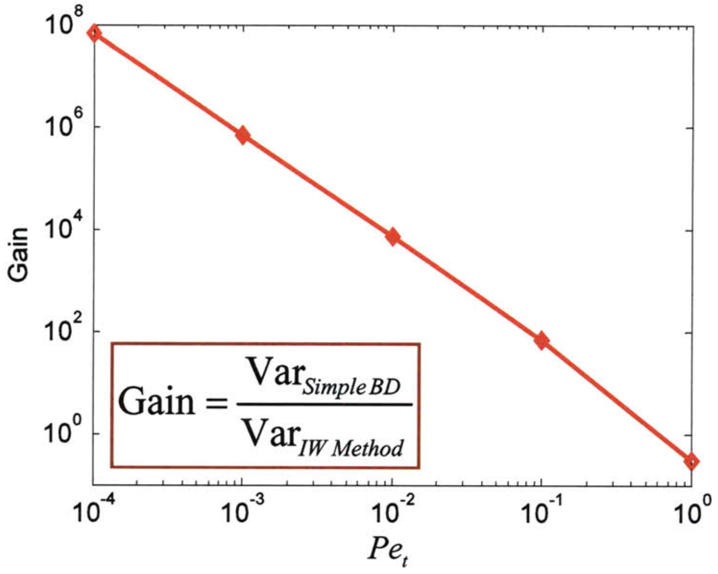

Figure 6-11: Comparing variances of importance-weight method and regular Brownian Dynamics.

6.6.3 Advantages and limitations of importance-weight method

The proposed importance-weight method provides great variance reduction for small translational Péclet number $Pe_t \ll 1$. It is easy to use and implement for 1, 2 and 3D problems. The computational overhead is minimal and it only requires the calculation of one weight for every particle at every time step.

The method relies on analytical solution for the transition probabilities. (This is, in fact, one of the limitations of the method). In addition, for larger simulations (e.g. larger devices) one might need to include a stabilization scheme, since weights eventually grow resulting in loss of variance reduction (this can be explained as loss of correlation between the two simulations [38, 45]); stabilization schemes for this have been developed [45], but they are rather cumbersome in the case of Brownian Dynamics simulations and detract from the simplicity (and efficiency) of the method, making it less attractive. In our simulation a stabilization scheme is not required since the simulation time is relatively short.

Chapter 7

Conclusions and outlook

In this Thesis, we have developed a number of computational models for simulating the low-field electrokinetic separation of biological molecules using nanoscale sieving devices. Our modeling efforts focused on the Ogston regime where molecule characteristic lengths are on the order of, or smaller than, the device pore size. Considerable effort has been expended in producing accurate numerical models that are in *quantitative* agreement with experimental data; specifically our simulations are validated using the experimental data of Fu et al. [4]. Three Brownian Dynamics (BD) simulation models have been developed.

The first, most general, formulation is based on the Worm-Like-Chain (WLC) model which includes the effects of bending and stretching stiffness and provides the most accurate description for the DNA molecule. Our implementation of the Worm-Like-Chain model is in line with the work of Allison et al., Hagerman et al., Lewis et al, Klenin et al. [34, 35, 36, 37] with a new discretization that treats all beads equally and is different from Bead-Spring models typically used for long molecules [38, 39]. The resulting Brownian Dynamics formulation includes hydrodynamic interactions between beads, and closely models the experimental setup of Fu et al. [4] whose data we used for validation. The model captures the transition in drag behavior between rigid rod and long chains (Zimm model) and describes moderate-size DNA electrophoresis (up to 340 nm (950 bp)).

The second model exploits the fact that short molecules can be treated as rigid, enabling the more efficient rigid-rod Brownian Dynamics algorithm to be used. The resulting simulation method method is more efficient (by a factor of four or more) than the WLC implementation described above. Comparison with the WLC simulation results and experimental data shows that it is accurate for molecule lengths on the order of, or smaller than, one persistence length, as expected.

The third model is even more computationally efficient. This is achieved by exploiting the fact that for sufficiently short molecules under the experimental conditions of interest, the rotational degrees of freedom of molecules can be treated by equilibrium partition coefficients. Under this treatment, first proposed by Li et al. within a Fokker-Planck framework [41], the partition coefficients can be used to quantify the number of configurations that are not accessible to the molecule and thus describe the entropic barrier associated with molecular motion in sieving devices. This allows the treatment of molecules as Brownian particles subject to an entropic barrier, which is significantly more efficient than the previous two formulations. Comparison with experimental results and rigid-rod Brownian Dynamics simulations shows that, provided the molecules are sufficiently short for the rigid-rod assumption to be valid, no significant error is introduced by these additional approximations.

Due to the advances in manufacturing, one will be able to precisely control the dimensions of the nanofluidic devices. The different BD models presented in this work are very useful for gaining fundamental understanding of the separation process, optimization, and parameter exploration. The models presented here are sufficiently accurate for use in the design of new separation devices with more elaborate geometries, such as the device featuring a two-dimensional geometry for continuous separation [3]. In Chapter 3, we used our WLC model to verify the analytical predictions of Li et al. [41] for an asymmetric device in the presence of an electric field of alternating polarity. It is of great interest to further pursue this research direction by using our numerical models to explore different sieving patterns and electric field regimes in order to improve biomolecule separation. In order to have a more accurate comparison with experimental data, it is essential to have more a precise characterization of the actual system geometry, as well as more accurate characterization of other system parameters (e.g. electroosmotic flow magnitude).

The numerical models presented here were applied to dsDNA molecules; extending these models to other biological molecules is essential. Furthermore, our numerical effort focused on modeling the separation process in the Ogston-sieving regime; extending our numerical effort to model the transition region between Ogston-Entropic sieving and even further to *quantitatively* model the entropic sieving process is essential in the development of fast and accurate micro-nanofluidic sieving devices.

Finally, the variance reduction methods presented here (Chapter 6) are the first attempts to decrease the variance of Brownian Dynamics simulations in the presence of solid boundaries. We showed that the importance-weight method provides great variance reduction for low translational Péclet numbers and is easy to implement requiring little additional computational cost. Our implementation was limited to non-interacting point particles; further work is necessary to extend this method to rigid-rod and Worm-Like-Chain models. One approach toward this goal would be a direct extension of the present work which would require an analytical or inexpensive numerical solution for the transitional probabilities of a rigid-rod and Worm-Like-Chain model near one wall.

Bibliography

[1] T. T. Duong, G. Kim, R. Ros, M. Streek, F. Schmid, J. Brugger, D. Anselmetti, and A. Ros. Size-dependent free solution DNA electrophoresis in structured microfluidic systems. *Microelectronic Engineering*, 67:905–912, 2003.

[2] W. D. Volkmuth and R. H. Austin. DNA electrophoresis in microlithographic arrays. 1992.

[3] J. Fu, R. B. Schoch, A. L. Stevens, S. R. Tannenbaum, and J. Han. A patterned anisotropic nanofluidic sieving structure for continuous-flow separation of DNA and proteins. *Nature Nanotechnology*, 2:121–128, 2007.

[4] J. Fu, J. Yoo, and J. Han. Molecular sieving in periodic free-energy landscapes created by patterned nanofilter arrays. *Physical Review Letters*, 97(1):018103, 2006.

[5] O. Kratky and G. Porod. Röntgenuntersuchung gelöster fadenmoleküle. *Recueil des Travaux Chimiques des Pays-Bas-Journal of the Royal Netherlands Chemical Society*, 68(12):1106–1122, 1949.

[6] J. F. Marko and E. D. Siggia. Stretching DNA. *Macromolecules*, 28(26):8759–8770, 1995.

[7] G. L. Lukacs, P. Haggie, O. Seksek, D. Lechardeur, N. Freedman, and A. S. Verkman. Size-dependent DNA Mobility in Cytoplasm and Nucleus. *Journal of Biological Chemistry*, 275(3):1625–1629, 2000.

[8] H. C. Öttinger, B. H. A. A. Van Den Brule, and M. A. Hulsen. Brownian configuration fields and variance reduced CONNFFESSIT. *Journal of Non-Newtonian Fluid Mechanics*, 70(3):255–261, 1997.

[9] G. B. Smejkal and A. Lazarev (eds.). *Separation methods in proteomics.* CRC Taylor & Francis, Boca Raton, FL, 2006.

[10] J. C. Giddings. *Dynamics of Chromatography. Part 1. Principles and Theory.* Marcel Dekker, New York, 1965.

[11] R. K. Scopes. *Protein purification: principles and practice.* Springer-Verlag, New York, 1994.

[12] P. Gill. DNA as evidence – the technology of identification. *New England Journal of Medicine*, 352(26):2669–2671, 2005.

[13] Varsha. DNA fingerprinting in the criminal justice system: An overview. *DNA and Cell Biology*, 25(3):181–188, 2006.

[14] D. Fliser, S. Wittke, and H. Mischak. Capillary electrophoresis coupled to mass spectrometry for clinical diagnostic purposes. *Electrophoresis*, 26(14):2708–2716, 2005.

[15] L. Lam, J. Lind, and C. Semsarian. Application of proteomics in cardiovascular medicine. *International Journal of Cardiology*, 108(1):12–19, 2006.

[16] T. Hirano and H. Kato. Present status of clinical proteomic analysis for the early detection and determination of therapeutic strategy in lung cancer. *Annals of Thoracic and Cardiovascular Surgery*, 12(1):4–9, 2006.

[17] J. Han and H. G. Craighead. Separation of long DNA molecules in a microfabricated entropic trap array. *Science*, 288(5468):1026–1029, 2000.

[18] J. Fu, P. Mao, and J. Han. Nanofilter array chip for fast gel-free biomolecule separation. *Applied Physics Letters*, 87(26):263902, 2005.

[19] N. Laachi, C. Declet, C. Matson, and K. D. Dorfman. Nonequilibrium transport of rigid macromolecules in periodically constricted geometries. *Physical Review Letters*, 98(9):098106, 2007.

[20] M. Streek, F. Schmid, T. T. Duong, and A. Ros. Mechanisms of DNA separation in entropic trap arrays: a Brownian Dynamics simulation. *Journal of Biotechnology*, 112(1-2):79–89, 2004.

[21] S. H. Kim, A. S. Panwar, S. Kumar, K. H. Ahn, and S. J. Lee. Electrophoresis of a bead-rod chain through a narrow slit: A Brownian Dynamics study. *Journal of Chemical Physics*, 121(18):9116–9122, 2004.

[22] D. Duong-Hong, J. Han, J. Wang, N. G. Hadjiconstantinou, Y. Z. Chen, and G. Liu. Realistic simulations of combined DNA electrophoretic flow and eof in nano-fluidic devices. *Electrophoresis*, 29(24):4880–4886, 2008.

[23] A. S. Panwar and S. Kumar. Time scales in polymer electrophoresis through narrow constrictions: A Brownian Dynamics study. *Macromolecules*, 39(3):1279–1289, 2006.

[24] M. P. Allen and D. J. Tildesley. *Computer Simulation of Liquids.* Oxford University Press, USA, June 1989.

[25] D. L. Ermak and J. A. McCammon. Brownian Dynamics with hydrodynamic interactions. *The Journal of Chemical Physics*, 69(4):1352–1360, 1978.

[26] P. S. Grassia, E. J. Hinch, and L. C. Nitsche. Computer-simulations of Brownian-Motion of complex-systems. *Journal of Fluid Mechanics*, 282:373–403, 1995.

[27] P. Espanol. Statistical mechanics of coarse-graining. *Novel Methods in Soft Matter Simulations*, pages 2256–2256, 2003.

[28] T. Schlick. *Molecular modeling and simulation.* Springer New York, 2002.

[29] G. W. Slater, C. Holm, M. V. Chubynsky, H. W. de Haan, A. Dubé, K. Grass, O. A. Hickey, C. Kingsburry, D. Sean, T. N. Shendruk, and L. Zhan. Modeling the

separation of macromolecules: A review of current computer simulation methods. *Electrophoresis*, 30(5):792–818, 2009.

[30] R. M. Jendrejack, M. D. Graham, and J. J. De Pablo. Hydrodynamic interactions in long chain polymers: Application of the Chebyshev polynomial approximation in stochastic simulations. *The Journal of Chemical Physics*, 113:2894, 2000.

[31] M. Fixman. Construction of Langevin forces in the simulation of hydrodynamic interaction. *Macromolecules*, 19:1204–1207, 1986.

[32] J. P. Hernández-Ortiz, J. J. de Pablo, and M. D. Graham. Fast computation of many-particle hydrodynamic and electrostatic interactions in a confined geometry. *Physical Review Letters*, 98(14):140602, 2007.

[33] R. M. Jendrejack, E. T. Dimalanta, D. C. Schwartz, M. D. Graham, and J. J. de Pablo. DNA dynamics in a microchannel. *Physical Review Letters*, 91(3):38102, 2003.

[34] K. Klenin, H. Merlitz, and J. Langowski. A Brownian Dynamics program for the simulation of linear and circular DNA and other wormlike chain polyelectrolytes. *Biophysical Journal*, 74(2):780–788, 1998.

[35] S. A. Allison. Brownian Dynamics simulation of wormlike chains - fluorescence depolarization and depolarized light-scattering. *Macromolecules*, 19(1):118–124, 1986.

[36] R. J. Lewis, S. A. Allison, D. Eden, and R. Pecora. Brownian Dynamics simulations of a three-subunit and a ten-subunit worm-like chain: Comparison of results with trumbell theory and with experimental results from DNA. *The Journal of Chemical Physics*, 89(4):2490–2503, 1988.

[37] P. J. Hagerman and B. H. Zimm. Monte Carlo approach to the analysis of the rotational diffusion of wormlike chains. *Biopolymers*, 20(7):1481–1502, 1981.

[38] H. C. Öttinger. *Stochastic Processes in Polymeric Fluids: Tools and Examples for Developing Simulation Algorithms.* Springer, Berlin ; New York, 1996.

[39] M. Somasi, B. Khomami, N. J. Woo, J. S. Hur, and E. S. G. Shaqfeh. Brownian Dynamics simulations of bead-rod and bead-spring chains: numerical algorithms and coarse-graining issues. *Journal of Non-Newtonian Fluid Mechanics*, 108(1-3):227–255, 2002.

[40] Y. Tao, W. K. Den Otter, J. T. Padding, J. K. G. Dhont, and W. J. Briels. Brownian Dynamics simulations of the self- and collective rotational diffusion coefficients of rigid long thin rods. *The Journal of Chemical Physics*, 122(24):244903, 2005.

[41] Z. R. Li, G. R. Liu, J. Han, Y. Cheng, Y. Z. Chen, J. Wang, and N. G. Hadjiconstantinou. Analytical description of ogston-regime biomolecule separation using nanofilters and nanopores. *Physical Review E*, 80(4):041911, Oct 2009.

[42] L. L. Baker and N. G. Hadjiconstantinou. Variance-reduced Monte Carlo solutions of the Boltzmann equation for low-speed gas flows: A discontinuous Galerkin formulation. *International Journal for Numerical Methods in Fluids*, 58(4):381–402, 2008.

[43] L. L. Baker and N. G. Hadjiconstantinou. Variance-reduced particle methods for solving the Boltzmann equation. *Journal of Computational and Theoretical Nanoscience*, 5(2):165–174, 2008.

[44] H. A. Al-Mohssen and N. G. Hadjiconstantinou. Low-variance direct Monte Carlo using importance weights. *Mathematical Modelling and Numerical Analysis*, In Press, 2010.

[45] H. A. Al-Mohssen. *An Excursion with the Boltzmann Equation at Low Speeds: Variance-Reduced DSMC.* PhD thesis, Massachusetts Institute of Technology, 2010.

[46] C. Hsieh, A. Balducci, and P. S. Doyle. Ionic effects on the equilibrium dynamics of DNA confined in nanoslits. *Nano Letters*, 8(6):1683–1688, 2008.

[47] Prince E. Rouse Jr. A theory of the linear viscoelastic properties of dilute solutions of coiling polymers. *The Journal of Chemical Physics*, 21(7):1272–1280, 1953.

[48] M. Doi and S. F. Edwards. *The Theory of Polymer Dynamics (The International Series of Monographs on Physics)*. Oxford University Press, USA, November 1988.

[49] B. H. Zimm. Dynamics of polymer molecules in dilute solution: Viscoelasticity, flow birefringence and dielectric loss. *The Journal of Chemical Physics*, 24(2):269–278, 1956.

[50] B. Ilic, Y. Yang, K. Aubin, R. Reichenbach, S. Krylov, and H.G. Craighead. Enumeration of DNA molecules bound to a nanomechanical oscillator. *Nano Letters*, 5(5):925–929, 2005.

[51] A. E. Nkodo, J. M. Garnier, B. Tinland, H. Ren, C. Desruisseaux, L. C. McCormick, G. Drouin, and G. W. Slater. Diffusion coefficient of DNA molecules during free solution electrophoresis. *Electophoresis*, 22(12):2424–2432, 2001.

[52] H. Benoit and P. Doty. Light scattering from non-Gaussian chains. *The Journal of Physical Chemistry*, 57(9):958–963, 1953.

[53] J. Happel and H. Brenner. *Low Reynolds number hydrodynamics: with special applications to particulate media*. Kluwer Academic Print on Demand, 1991.

[54] C. Hirsch. *Numerical computation of internal & external flows: fundamentals of numerical discretization*. John Wiley & Sons, Inc., 1988.

[55] N. Sharma and N. A. Patankar. Direct numerical simulation of the Brownian Motion of particles by using fluctuating hydrodynamic equations. *Journal of Computational Physics*, 201(2):466–486, 2004.

[56] P. J. Hoogerbrugge and J. M. V. A. Koelman. Simulating microscopic hydrodynamic phenomena with dissipative particle dynamics. *Europhysics Letters*, 19(3):155–160, 1992.

[57] S. Succi. *The lattice Boltzmann equation for fluid dynamics and beyond.* Numerical mathematics and scientific computation. Clarendon Press ; Oxford University Press, Oxford, New York, 2001.

[58] G. N. Fayad and N. G. Hadjiconstantinou. Realistic Brownian Dynamics simulations of biological molecule separation in nanofluidic devices. *Microfluidics and Nanofluidics*, 8(4):521–529, 2010.

[59] Y. Lu, B. Weers, and N. C. Stellwagen. DNA persistence length revisited. *Biopolymers*, 61(4):261–275, 2002.

[60] J. Rotne and S. Prager. Variational treatment of hydrodynamic interaction in polymers. *The Journal of Chemical Physics*, 50(11):4831–4837, 1969.

[61] J. Han and H. G. Craighead. Characterization and optimization of an entropic trap for DNA separation. *Analytical Chemistry*, 74(2):394–401, 2002.

[62] D. Long, J. Viovy, and A. Ajdari. Stretching DNA with electric fields revisited. *Biopolymers*, 39(6):755–759, 1996.

[63] D. Long, J. Viovy, and A. Ajdari. Simultaneous action of electric fields and nonelectric forces on a polyelectrolyte: Motion and deformation. *Physical Review Letters*, 76(20):3858 LP - 3861, 1996.

[64] R. K. Pathria. *Statistical Mechanics, Second Edition.* Butterworth-Heinemann, July 1996.

[65] N. C. Stellwagen, C. Gelfi, and P. G. Righetti. The free solution mobility of DNA. *Biopolymers*, 42(6):687–703, 1997.

[66] S. B. Smith and A. J. Bendich. Electrophoretic charge density and persistence length of DNA as measured by fluorescence microscopy. *Biopolymers*, 29(8-9):1167–1173, 1990.

[67] Z. R. Li, G. R. Liu, J. Han, Y. Z. Chen, J. Wang, and N. G. Hadjiconstantinou. Transport of biomolecules in asymmetric nanofilter arrays. *Analytical and Bioanalytical Chemistry*, 394(2):427–435, 2009.

[68] M. M. Tirado, C. L. Martinez, and J. G. de La Torre. Comparison of theories for the translational and rotational diffusion coefficients of rod-like macromolecules. application to short DNA fragments. *The Journal of Chemical Physics*, 81(4):2047–2052, 1984.

[69] D. Long, A. V. Dobrynin, M. Rubinstein, and A. Ajdari. Electrophoresis of polyampholytes. *The Journal of Chemical Physics*, 108(3):1234–1244, 1998.

[70] S. A. Allison, C. Chen, and D. Stigter. The length dependence of translational diffusion, free solution electrophoretic mobility, and electrophoretic tether force of rigid rod-like model duplex DNA. *Biophysical Journal*, 81(5):2558–2568, 2001.

[71] Z. R. Li, G. R. Liu, Y. Z. Chen, J. Wang, H. Bow, Y. Cheng, and J. Han. Continuum transport model of ogston sieving in patterned nanofilter arrays for separation of rod-like biomolecules. *Electrophoresis*, 29(2):329–339, 2008.

[72] J. C. Giddings, E. Kucera, C. P. Russell, and M. N. Myers. Statistical theory for the equilibrium distribution of rigid molecules in inert porous networks. exclusion chromatography. *J. Phys. Chem.*, 72(13):4397–4408, 1968.

[73] A. Ajdari and J. Prost. Free-flow electrophoresis with trapping by a transverse inhomogeneous field. *Proceedings of the National Academy of Sciences of the United States of America*, 88(10):4468–4471, 1991.

[74] H. Brenner and D. A. Edwards. *Macrotransport Processes (Butterworth.* Butterworth-Heinemann Series in Chemical Engineering, Stoneham, MA, 1993.

[75] Z. R. Li, G. R. Liu, N. G. Hadjiconstantinou, J. Han, J. Wang, and Y. Z. Chen. Dispersive transport of biomolecules in periodic energy landscapes with application to nanofilter sieving arrays. *To be published.*

[76] M. Melchior and H. C. Öttinger. Variance reduced simulations of polymer dynamics. *The Journal of Chemical Physics*, 105(8):3316–3331, 1996.

[77] E. Peters and T. M. Barenbrug. Efficient Brownian dynamics simulation of particles near walls. I. Reflecting and absorbing walls. *Physical Review E*, 66(5):56701, 2002.

[78] M. V. Smoluchowski. Three presentations on diffusion, molecular movement according to Brown and coagulation of colloid particles. *Physikalische Zeitschrift*, 17:557–571, 1916.

[79] M. V. Smoluchowski. Three lectures on diffusion, Brown's molecular movements and the coagulation of colloid parts. *Physikalische Zeitschrift*, 17:585–599, 1916.